International Journal of Solids and Structures 200–201 (2020) 34–63

Contents lists available at ScienceDirect

International Journal of Solids and Structures

journal homepage: www.elsevier.com/locate/ijsolstr

Use of loss limit approach to zero in scattering-based parameter retrieval of elastic micro-structured media

Reza Abedi [a,*], Alireza V. Amirkhizi [b]

[a] Department of Mechanical Aerospace and Biomedical Engineering, University of Tennessee Space Institute/Knoxville, 411 B.H. Goethert Pkwy, Tullahoma, TN 37388, USA
[b] Department of Mechanical Engineering, University of Massachusetts Lowell, 1 University Ave., Lowell, MA 01854 USA

ARTICLE INFO

Article history:
Received 22 October 2019
Received in revised form 27 March 2020
Accepted 9 May 2020
Available online 21 May 2020

Keywords:
Parameter retrieval method
Dynamic overall properties
Homogenization
Material loss
Damping
Discontinuous Galerkin

ABSTRACT

The parameter retrieval method based on scattering data is used to derive dynamic constitutive parameters of solids with periodic structure. There are inherent ambiguities in the real part of the retrieved wavenumber and the sign of impedance, though the latter has a one-to-one correspondence with the direction of energy flux. Moreover, for lossless structures there can be multiple solution branches that satisfy passivity and continuity of the wavenumber as a function of frequency, leading to potentially double positive or double negative (in terms of density and modulus) overall descriptions of the micro-structured medium. The continuity of wavenumber for lossy unit cells is used to unambiguously determine their constitutive parameters and by taking the limit when loss approaches zero, one can determine the stable solution branches of lossless micro-structures. The two loss models of nonzero damping and complex modulus are compared in terms of their energy loss characteristics and retrieved parameters. These models are employed in both time and frequency domain calculations. The lossy solutions demonstrate that from double-negative and double-positive solutions, only the latter is the stable solution branch in a pass-band of a lossless 1D unit cell. A 2D photonic crystal example is used to demonstrate that the wavenumber appears to jump, discontinuously, at the transition point between two consecutive stop-bands, hence rendering the existing methods based on continuity of wavenumber ineffective. In contrast, the proposed approach based on taking limit of lossy solutions can successfully be used to determine stable overall properties of such media. Finally, certain features of half- and full-cycle stop-bands are discussed.

Published by Elsevier Ltd.

1. Introduction

As described in Srivastava (2015), for *quasi-static regime*, *i.e.,* when the characteristic size of the unit cell of a periodic structure, l, is much smaller than the wavelength λ, traditional static homogenization approaches (Nemat-Nasser and Hori, 2013) can be used to represent the overall behavior of the micro-structured medium. In contrast for the *short wavelength* regime, the heterogeneous material response *cannot* be represented by effective bulk constitutive models. Our interest is in *intermediate/long wave length* limit, where the ratio λ/l is a finite quantity of order 1. Needless to say, this approach is also applicable to cases when λ/l becomes large, *i.e.,* the long wavelength limit. Under such circumstances material response can be modeled by *effective constitutive parameters* which are frequency-dependent, *i.e.,* dispersive.

In solid mechanics several approaches are proposed to model dynamic effects in the intermediate regime. In a (quasi) static regime and in the absence of inertia terms the Hill-Mandel energy equivalency between micro and macro scales enables the definition of *Representative Volume Element* (RVE) and derivation of macroscopic effective parameters. In Wang and Sun (2002) Hill-Mandel condition is extended to dynamic regime by adding source terms at macroscale that preserve energy equivalency. In general, full dynamic coupling between computational models at micro and macro scales is quite challenging. Accordingly, several approaches with different levels of dynamic coupling and fidelity are proposed. In the context of computational homogenization methods, a limited dynamic coupling between macroscale and RVEs at finite element quadrature points is formulated in Pham et al. (2013). The majority of asymptotic expansion methods, *e.g.,* (Santosa and Symes, 1991; Andrianov et al., 2008; Auriault et al., 2010, solve a dynamic problem only at macroscale. In Craster et al., 2010; Hui and Oskay, 2013; Hui and Oskay, 2014; Hui and Oskay, 2015) homogenization is formulated at fixed frequencies.

* Corresponding author.
E-mail addresses: rabedi@utk.edu (R. Abedi), alireza_amirkhizi@uml.edu (A.V. Amirkhizi).

https://doi.org/10.1016/j.ijsolstr.2020.05.010
0020-7683/Published by Elsevier Ltd.

Some of these methods expand to third or higher order asymptotic terms for increased accuracy and applicability, for example to model two-phase (Boutin and Auriault, 1993) and three-phase (Auriault and Boutin, 2012) composites with potentially high contrast ratio of elastic moduli of different phases.

Another approach is the derivation of dispersive effective constitutive parameters that can subsequently be directly used in macroscopic dynamic simulations. In *frequency domain* (FD) this involves modeling a unit cell (or RVE) at fixed frequencies to derive these dispersive constitutive parameters. The derivation of such dispersive properties has traditionally been focused on field averaging techniques; *cf.* (Smith et al., 2000; Smith and Pendry, 2006; Lerat et al., 2006; Amirkhizi and Nemat-Nasser, 2008; Pors and Bozhevolnyi, 2011 for electromagnetic and Willis, 2009; Nemat-Nasser et al., 2011; Willis, 2011; Srivastava and Nemat-Nasser, 2011; Norris et al., 2012) for elastodynamic examples. By computing the averages of the (periodic part of the) fields on the left-hand and right-hand sides of a constitutive relation, the parameters of the constitutive equation can be derived.

The *parameter retrieval method* is another method that can characterize dispersive properties of composites at the intermediate wavelength regime. In these methods the scattering (S) parameters of a finite samples are experimentally or computationally measured. Next, effective properties for the material are sought such that the scattering parameters for the same width of effective medium match those of the original sample. While field averaging methods are often preferred to computationally characterize complex 2D and 3D geometries, the use of parameter retrieval methods is prevalent in experimental settings. This is due to the lack of access to micro-scale field quantities in the laboratory (Amirkhizi, 2017) and relative ease in experimentally measuring scattering parameters. This method is used in computational electromagnetics (Smith et al., 2002; Markoš and Soukoulis, 2003; Chen et al., 2004; Liu et al., 2007; Smith et al., 2005; Chen et al., 2005; Arslanagić et al., 2013; Hasar et al., 2015) and acoustics (Fokin et al., 2007; Wang et al., 2008; Zhu et al., 2012). For elastodynamics, while not used for equivalent constitutive modeling, S-parameters are studied in Merheb et al. (2008), Dontsov et al. (2013), Wautier and Guzina (2015), Sadeghi et al. (2013) among others.

For dispersive materials both spatial and temporal dispersions can be modeled through the dependency of overall properties on wave vector $\mathbf{k}$ and angular frequency ω, respectively. Some examples can be found in Hui and Oskay (2014), Meng and Guzina (2018), Guzina et al. (2019) for the asymptotic methods and Silveirinha (2011) for the field averaging method. For these methods, the excitation of the unit cell is often in the form of a source term that depends on both $\mathbf{k}$ and ω. However, homogenizing to overall properties that are only temporally dispersive is more common in the literature. For materials that would require gradient elasticity theory as their constitutive equation (Hui and Oskay, 2014) incorporates both spatial and temporal dispersion. For the remainder of this paper, we only consider temporal dispersion in which overall properties depend solely on ω. For further discussion on the class of problems that may require both spatial and temporal dispersions and the relation between the two models, we refer the readers to Silveirinha (2011).

In this paper, dispersive overall (or apparent) properties of symmetric unit cells are derived based on the parameter retrieval method. Specifically, we use a robust approach proposed in Amirkhizi (2017) to characterize layered media. It is shown that by adding loss to a unit cell and taking the limit of retrieved dispersive parameters as loss goes to zero, properties of the lossless unit cell can be unambiguously determined. It must be noted, the work presented here focuses on regions of frequency and wave vector spaces, where such an overall wave dynamics description is suitable. It is likely that such a description is not suitable, for example, near Dirac cones or other singularities of the band structure (*e.g.,* exceptional points). We note, however, that simple crossings of band structure, *e.g.,* when shear modes and longitudinal modes have the same wavelength and frequency, do not necessarily interfere with this analysis as mentioned briefly in Section 5.3, where the shear mode is shown to cross the longitudinal mode (based on eigenvalue band structure calculations), but the longitudinal parameter extraction method for longitudinal waves is not at all affected.

There is an inherent non-uniqueness in the parameter retrieval method, in that the transmission phase change, *i.e.,* the product of the real part of the wavenumber by the slab length, can only be determined by up to arbitrary additions of full circle angle. That is, p, the number of full cycle waves in the effective domain cannot be uniquely determined. A general approach is the characterization of the sample from low enough frequencies for which the number of full wave cycles is zero. Then, continuity of certain quantities, *e.g.,* the wavenumber k, is used to unambiguously March the parameter retrieval method forward to higher frequencies. As shown in Arslanagić et al. (2013), by assigning an incorrect value for p, the properties at a given frequency can erroneously be characterized as double positive, single positive, or even double negative. The characterization of lossless unit cells is even more challenging, since there can be multiple *valid* solution branches for which the aforementioned continuity constraints are satisfied. There is an inherent non-uniqueness in the parameter retrieval method, in that the transmission phase change, *i.e.,* the product of the real part of the wavenumber by the slab length, can only be determined by up to arbitrary additions of full circle angle. That is, p, the number of full cycle waves in the effective domain cannot be uniquely determined. A general approach is the characterization of the sample from low enough frequencies for which the number of full wave cycles is zero. Then, continuity of certain quantities, *e.g.,* the wavenumber k, is used to unambiguously March the parameter retrieval method forward to higher frequencies. As shown in Arslanagić et al. (2013), by assigning an incorrect value for p, the properties at a given frequency can erroneously be characterized as double positive, single positive, or even double negative. The characterization of lossless unit cells is even more challenging, since there can be multiple *valid* solution branches for which the aforementioned continuity constraints are satisfied.

In this paper, dispersive overall (or apparent) properties of symmetric unit cells are derived based on the parameter retrieval method. Furthermore, we use a robust approach proposed in Amirkhizi (2017) to characterize layered media. It is shown that by adding loss to a unit cell and taking the limit of retrieved dispersive parameters as loss goes to zero, properties of the lossless unit cell can be unambiguously determined.

Since the constitutive parameters of dispersive materials are expressed as functions of frequency ω, FD methods appear to be the natural choice for their characterization. However, *time domain* (TD) methods have the ability to characterize dispersive properties for a wide range of frequencies with just one simulation, and in some cases they have been reported to be more efficient that FD methods; see for example (Silveirinha, 2011; Chan et al., 1995; Niegemann et al., 2009). Herein, we also compare two different methods to introduce loss to a unit cell; for TD methods loss is often introduced by using a nonzero damping parameter, whereas for FD methods a complex modulus is typically used. We show that the limiting process can be applied in both time and frequency domains and is relatively independent of the way loss is introduced.

The outline of the paper is as follows. In Section 2 the parameter retrieval method and the ambiguities involved in the value of p and sign of impedance are described. In Section 3 the two loss models are compared in terms of their energy loss characteristics and

accuracy in retrieved constitutive parameters relative to a lossless homogeneous material. In Section 4 several 1D layered unit cells are characterized and the form of the retrieved parameters in stop-bands and pass-bands are discussed. Further, the two loss models are compared and used to determine the *stable* solution branches. Specifically, by using lossy solutions, it is shown that from two valid double positive and double negative solutions of retrieved parameters in a pass-band, only the double positive solution is stable. Next, the 2D unit cell in Section 5 is used to elaborate on some solution features that were not encountered for 1D unit cells. Specifically, it is shown that the wavenumber can in fact suffer jumps in lossless micro-structures. The use of lossy unit cells can robustly handle this more complex problem, whereas the retrieval methods that are based on the continuity of k would fail. The approach described in this paper is suitable when the ratio λ/l is a finite quantity of order 1, as well as in the long wavelength limit when it is a large quantity. The final conclusions are drawn in Section 6.

2. Parameter retrieval method

In this section, we discuss the derivation of effective material parameters for 1D and 2D unit cells using the parameter retrieval method. This process is shown in Fig. 1. The scattering parameters of a unit cell can be obtained using different approaches, as conceptually shown in Fig. 1(a). In Section 2.1, matching and propagation matrices are used to analytically derive scattering parameters for a 1D multi-layer unit cell for an arbitrary frequency ω. *Time domain* (TD) and *frequency domain* (FD) approaches are discussed in Section 2.3 to derive scattering parameters of 2D unit cells.

Once the scattering parameters are determined for a given angular frequency ω, effective properties are sought such that the scattering parameters of the unit cell, formed by uniform effective properties, matches those of the unit cell. The concept of effective properties is shown in Fig. 1(b) and discussed in Section 2.1. The inverse problem for the derivation of these effective properties, shown in Fig. 1(c), is discussed in Section 2.2.

2.1. Scattering parameters for 1D multi-layer unit cells

We aim to obtain the scattering matrix for the m-layer 1D unit cell shown in Fig. 2. Beside its use for analytical derivation of scattering properties for 1D multi-layer unit cells in Section 4.1 to Section 4.3, this approach is the basis to derive effective properties in Section 2.2. The length, impedance, and wave speed of layer j are l_j, Z_j, and c_j, respectively. The stress values for the right- and left-going waves on the left side of the layer j are denoted by σ^+_{jl} and σ^-_{jl}, respectively. The same values on the right side of layer j are denoted by σ^+_{jr} and σ^-_{jr}. The constitutive parameters of layer j are mass density $\rho_j = Z_j/c_j$ and modulus $C_j = Z_j c_j$. The ambient medium on the left side of the unit cell has the impedance Z_0, whereas the impedance on the right side of interface $m+1$ is Z_{m+1}. To satisfy the continuity of displacements and tractions from the two sides of this m-layer unit cell, we use matching and propagating matrices. The *matching matrix* of interface j, $\mathbf{M}_j$, relates the stress values from the left and right sides of interface j (Orfanidis, 2014),

$$\begin{bmatrix}\sigma^+_{(j-1)r}\\ \sigma^-_{(j-1)r}\end{bmatrix} = M_j \begin{bmatrix}\sigma^+_{jl}\\ \sigma^-_{jl}\end{bmatrix}, \quad \text{where} \quad M_j = \frac{1}{\tau_j}\begin{bmatrix}1 & \varrho_j\\ \varrho_j & 1\end{bmatrix}, \quad \text{and} \tag{1a}$$

$$\varrho_j = \frac{Z_j - Z_{j-1}}{Z_j + Z_{j-1}} \tau_j = \frac{2Z_j}{Z_j + Z_{j-1}} \tag{1b}$$

are reflection and transmission coefficients of the interface j, respectively, for a right-going wave. The stress values at the end points of slab j are related by the *propagating matrix*, $\mathbf{P}_j$,

$$\begin{bmatrix}\sigma^+_{jl}\\ \sigma^-_{jl}\end{bmatrix} = \mathbf{P}_j \begin{bmatrix}\sigma^+_{jr}\\ \sigma^-_{jr}\end{bmatrix}, \quad \text{where} \quad \mathbf{P}_j = \begin{bmatrix}\zeta_j & 0\\ 0 & \zeta_j^{-1}\end{bmatrix}, \quad \text{and} \quad \zeta_j = e^{k_j l_j} \tag{2}$$

where $k_j = \omega/c_j$ is the wavenumber corresponding to ω in layer j with wave speed c_j. We use the $e^{(\omega t - k_j x)}$ convention, where the wave is traveling to the right (in the sense of phase advance).

Using (1) for interfaces 1 to $m+1$ and (2) for layers 1 to m, we obtain the transfer matrix between the stresses at the two ends of the slab as,[1]

$$\begin{bmatrix}\sigma^+_{0r}\\ \sigma^-_{0r}\end{bmatrix} = \mathbf{T}\begin{bmatrix}\sigma^+_{(m+1)l}\\ \sigma^-_{(m+1)l}\end{bmatrix}, \quad \text{where} \quad \mathbf{T} = \mathbf{M}_1\mathbf{P}_1\cdots\mathbf{M}_{(m+1)} \tag{3}$$

Finally by considering a right-going wave, *i.e.*, $\sigma^-_{(m+1)l} = 0$, scattering coefficients of the slab are obtained as,

$$S_{21} = \frac{\sigma^+_{(m+1)l}}{\sigma^+_{0r}} = \frac{1}{T_{11}} \tag{4a}$$

$$S_{11} = \frac{\sigma^-_{0r}}{\sigma^+_{0r}} = \frac{T_{21}}{T_{11}} \tag{4b}$$

where S_{11} and S_{21} denote the reflection and transmission coefficients of a right-going wave. The left-going wave reflection S_{22} and transmission S_{12} coefficients can also be derived by inverting $\mathbf{T}$ and reversing the role of + and − waves.

In this paper, we limit ourselves to unit cells where scattering parameters are symmetric. The reflection and transmission coefficients of the unit cell are then unambiguously defined as $R := S_{11} = S_{22}$ and $T := S_{21} = S_{12}$; see Fig. 1(a, c) for the depiction of R and T. This condition is equivalent to $\det\mathbf{T} = 1$ and $T_{21} = -T_{12}$. Clearly, symmetry in geometry and material properties of the unit cell with respect to the y axis, *cf.* Fig. 1(a), ensures the symmetry of scattering properties of any given 1D or 2D unit cell. This symmetry includes the condition $Z_0 = Z_{m+1}$. Finally, the reflectance r, transmittance t, and absorbance a, defined by,

$$r = |R|^2 \qquad t = |T|^2 \qquad a = 1 - r - t \tag{5}$$

measure the portions of the energy that is reflected from, transmitted through, and absorbed in the unit cell. These energetic quantities are useful in analyzing the effect of added loss to lossless unit cells studied in subsequent sections.

2.2. Inverse problem for effective properties

As shown in Fig. 1(b), to derive equivalent properties, a unit cell with uniform properties Z, c is considered in an ambient medium with impedance $Z_0 = \sqrt{\rho_0 C_0}$. This corresponds to the 1D geometry in Fig. 2 with a single layer ($m = 1$), and ambient impedances $Z_2 = Z_0$. For simplicity, the subscripts of the first interface and layer are dropped. That is, for the first layer $\varrho := \varrho_1 = (Z - Z_0)/(Z + Z_0)$, and for the first layer, $Z := Z_1, c := c_1, k := \omega/c_1$. Using (1)–(4), the scattering parameters of a symmetric unit cell are derived as,

$$R = \varrho\frac{\zeta^2 - 1}{\zeta^2 - \varrho^2}, \quad T = \zeta.\frac{1 - \varrho^2}{\zeta^2 - \varrho^2} \tag{6}$$

The parameter $\zeta := \zeta_1$ is, *cf.* (2),

$$\zeta = e^{kl} \tag{7}$$

where $k = \omega/c$ is the wavenumber of wave in the medium and $l := l_1$ is the total length of the unit cell; *cf.* Fig. 1(a). It is noted that

[1] It is noted that the transfer matrices in this paper and in Amirkhizi (2017) are distinct and have different interpretations. However, the retrieved parameters are equivalent.

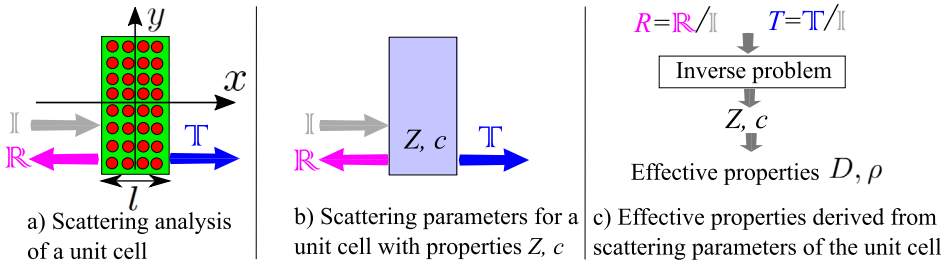

Fig. 1. Schematic of parameter retrieval method.

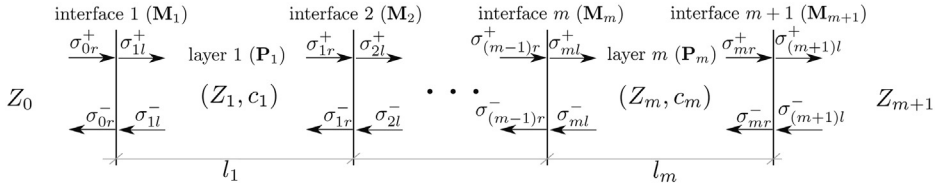

Fig. 2. Computing scattering parameters for an m-layer 1D unit cell in an ambient with impedance $Z_{m+1} = Z_0$.

the scattering parameters in (6) match the original values of the Nicolson-Ross-Weir method (Nicolson and Ross, 1970; Weir, 1974).

There are many studies on the inversion of (6) to obtain Z and c once R and T are known, see for example (Smith et al., 2002; Fokin et al., 2007; Shi et al., 2016). Herein a process given by Arslanagić et al. (2013) is followed where Z and ζ are given by,

$$Z = Z_0\sqrt{\frac{n}{d}}, \quad \text{where} \quad n := (R+1)^2 - T^2, \quad d := (R-1)^2 - T^2 \tag{8a}$$

$$\zeta = \frac{(Z+Z_0) - R(Z-Z_0)}{T(Z+Z_0)} \tag{8b}$$

The + and − signs in (8) a, correspond to the roots of $\sqrt{n/d}$ for which the real part of Z is positive and negative respectively; the root choices when $Z_r = 0$ will be discussed later. One observes that if (Z, ζ, k) satisfy (8), so does the set $(-Z, 1/\zeta, -k)$; see also (7). As will be discussed later, both sets of solutions result in the same effective material properties. Unlike the choice of sign of Z, there is an inherent ambiguity in deriving wavenumber k from ζ because of the phase ambiguity of log function; *i.e.,*

$$k = \frac{\phi}{l} - \frac{\log|\zeta|}{l}, \quad \text{where} \quad \phi := \theta + 2p\pi \tag{9}$$

and $|\zeta|$ and $\theta \in (-\pi, \pi]$ are used in polar expression of $\zeta = |\zeta|e^{\theta}$. In other words, the phase angle of kl is obtained only within arbitrary number of full waves traveling in the slab.

Before the discussion on the choice of p, we clarify how the sign of Z is chosen in (8) a. Based on the convention $e^{(\omega t - kx)}$ when ϕ is not an integer multiple of π, passivity requires $k_r k_i \leqslant 0$, where k_r and k_i are real and imaginary parts of k. The choices (Z, ζ, p, k) and $(Z, 1/\zeta, -p, -k)$ are the left- and right-moving waves that satisfy (8) and (9) (Arslanagić et al., 2013). We choose the set that corresponds to right-going waves (in the sense of phase velocity), as shown in Fig. 1(a, b). This stipulates $k_r \geqslant 0$ and $k_i \leqslant 0$. For a lossless unit cell, ϕ equal to an integer multiple of π corresponds to a standing wave for an infinite domain. For this case, the sign of k_i for $k_r > 0$ is chosen from the zero-loss limit solution of lossy unit cells which stipulates $k_i \leqslant 0$. Thus, the sign choice $k_r \geqslant 0$ and $k_i \leqslant 0$, referred to as right-going wave convention, is taken for all parameter retrieval cases from hereon. Since $k_i = -\log|\zeta|/l$ is unambiguously derived from (9), the sign of Z in (8) is determined when $k_i \neq 0$; *i.e.,* the root of Z is chosen such that it results in $k_i < 0$. The correct root corresponding to $k_i = 0$ is discussed below.

Thus, apart from the sign ambiguity of Z when $k_i = 0$, the only remaining unknown to determine k is p. One approach to resolve this non-uniqueness of p (and k_r) in the inverse problem is to start from low frequencies where $p = 0$ and as ω increases, determine the correct value of p by preserving the continuity of the wavenumber. A similar approach is taken in Shi et al. (2016) and Abedi and Mudaliar (2017) for electromagnetics problem. As long as k is a continuous function of ω, this approach can be used to correctly determine the frequencies for which p changes to ensure this continuity constraint. However, in Section 5, we show that this condition is violated for a 2D lossless photonic crystal.

Similar to Amirkhizi (2017), we propose the use of lossy unit cells to not only resolve the problem with continuity of $k(\omega)$, but also address the ambiguity in the sign of Z for frequencies for which $k_i = 0$. First, for lossy unit cells one should expect k to be a continuous function of ω, particularly in 1D wave propagation. The potential of mixed mode behavior complicates this expectation and requires further analysis. Moreover, for low enough loss values, one could expect extremely low transmission values within certain portions of the stop band which affects the numerical accuracy of the inversion procedure (using either computational results or experimental data). Nevertheless, one can always increase the loss value, without significantly altering the physical behavior of the structure, to reach a continuous dispersive k. Hence, this continuity constraint can be used to adjust p from its initial value of 0 at $\omega = 0$, as ω increases. Second, the two *valid* solutions of the lossless unit cells for $k_i = 0$ in pass-bands correspond to $(k_r > 0, k_i < 0)$ and $(k_r > 0, k_i > 0)$ for lossy unit cells. The solution branch corresponding to $(k_r > 0, k_i < 0)$ is referred to as the *stable* solution, as small disturbances to the lossless unit cell in the form of added loss result in a solution that is physically acceptable, satisfying passivity. Conversely, the latter solution branch is referred to as *unstable*. *The solutions for $Z(\omega)$ and $k(\omega)$ of a lossless unit cell are unambiguously determined as the limiting values of the corresponding solutions for lossy unit cells with $k_i < 0$ when the introduced loss parameter tends to zero.*

After k and Z are obtained, elastic constitutive parameters, compliance D and modulus C, are given by,

$$D = \frac{k}{Z\omega} \quad \Rightarrow C = \frac{1}{D} = \frac{Z\omega}{k} \tag{10a}$$

$$\rho = \frac{kZ}{\omega} \tag{10b}$$

The simultaneous appearance of k and Z in all retrieved constitutive parameters confirms that if (Z, ζ, p, k) is a valid retrieved set of parameters for a right-going wave, so is $(-Z, 1/\zeta, -p, -k)$ for a left-going wave. Finally, if the symmetry of scattering parameters discussed under (4) is not satisfied, the more general Willis-type constitutive equations (Milton and Willis, 2007; Willis, 2012) should have been employed to characterize the properties of the effective properties; see for example (Amirkhizi, 2017) for the use of parameter retrieval method for the more general Willis-type constitutive equations.

2.3. Computational derivation of scattering parameters

In this section, we will discuss how the scattering parameters are derived for a symmetric unit cell, in the sense defined below (4). Each layer is characterized with its constitutive parameters $\rho_j(\omega)$ and $C_j(\omega)$. We employ this method to analytically obtain scattering parameters for 1D unit cells considered in Section 4.1 to Section 4.3. The individual layers can be lossless or have loss in the form of having a nonzero damping coefficient or imaginary modulus $C_{j,i}(\omega)$, as discussed in Section 3.1.

For higher dimension unit cells we use a FD and a TD finite element method to numerically derive $R(\omega)$ and $T(\omega)$. For the FD approach, the commercial software COMSOL is used as described in Aghighi et al. (2019). For the TD analysis, the incident, transmitted, and reflected waves are all determined as functions of time. Upon the completion of the TD simulation, Fourier transform is applied on these waves to obtain their corresponding frequency-dependent functions. This facilitates the computation of scattering parameters for a wide range of frequencies.

The TD incident signal $\mathbb{I}(t)$ should satisfy a few conditions. First, it should have a rich FD representation to enable characterization of material for a wide range of frequencies. It also should be close to zero at initial time $t = 0$ and final time $t = \overline{T}$ so that the infinite limits of Fourier transform in time can be replaced with zero and $\overline{T}$. An incident wave in the form,

$$\mathbb{I}(t) = \sin(\omega_0 t) e^{-(t-t_0)^2/\varsigma^2} \tag{11}$$

with the Fourier transform,

$$\overline{\mathbb{I}}(\omega) = \frac{1}{2}\varsigma \exp(-\omega t_0)\left[e^{-\frac{\varsigma^2}{2}(\omega+\omega_0)^2} - e^{-\frac{\varsigma^2}{2}(\omega-\omega_0)^2}\right] \tag{12}$$

satisfies all these conditions, as discussed below. In (11), t_0 and ς are two time scales and ω_0 is a reference frequency. The most dominant frequency content of $\mathbb{I}(\omega)$ in (12) is $[\omega_{\min}, \omega_{\max}] = [\omega_0 - 1/\varsigma, \omega_0 + 1/\varsigma]$. Thus, ω_0 and ς can be obtained from the minimum and maximum frequencies of interest from $\omega_0 = 0.5(\omega_{\max} + \omega_{\min})$ and $\varsigma = 2/(\omega_{\max} - \omega_{\min})$. The role of t_0 is to ensure $\mathbb{I}(t) \approx 0$ close to the initial time $t = 0$. The time t_0 is assumed to be sufficiently large if it is at least three to four times larger than ς (Silveirinha, 2011; Busch et al., 2011). The final time $\overline{T}$ is chosen sufficiently large so that elastic waves withing and on the boundaries of the unit cell have attenuated sufficiently though the absorption in the unit cell, if applicable, and transmission and reflection from the right and left boundaries in Fig. 1(a). Thus, the Fourier transform for the reflected wave, can be approximated as follows,

$$\overline{\mathbb{R}}(\omega) = \frac{1}{\sqrt{2\pi}}\int_{-\infty}^{\infty} \mathbb{R}(t) e^{-\omega t} \mathrm{d}t \approx \frac{1}{\sqrt{2\pi}}\int_{0}^{\overline{T}} \mathbb{R}(t) e^{-\omega t} \mathrm{d}t \tag{13}$$

where $\mathbb{R}(t)$ is the spatial average of the reflected wave at time t. The details of the computation of $R(t)$ from a space and time dependent solution can be found in Abedi (2017). The same transformation can be used to compute $\overline{\mathbb{T}}(\omega)$ from $\mathbb{T}(t)$. Subsequently, reflection and transmission coefficients are computed from $R(\omega) = \overline{\mathbb{R}}(\omega)/\overline{\mathbb{I}}(\omega)$ and $T(\omega) = \overline{\mathbb{T}}(\omega)/\overline{\mathbb{I}}(\omega)$; *cf.* Fig. 1c) and 12. Note that $e^{-\omega t}$ kernel is used for Fourier transform for consistency with $e^{(\omega t - kx)}$ representation of planar waves and retrieved constitutive parameters in Section 2.2.

To computationally model the ambient zones on the left and right sides of the unit cell in Fig. 1(a), the computational domain is expanded beyond the unit cell on both reflection and transmission sides with ambient material. We use Silver-Müller condition to terminate the extended ambient zones at the far left and right sides of the computational domain. For the top and bottom sides of the domain we can use periodic boundary condition, but for the problems considered the unit cell is symmetric in the y-direction, facilitating the use of simpler boundary conditions that are implied by such symmetry. An alternative choice for boundaries of computational domain on the left and right based on Aghighi et al. (2019) is used for FD analysis, where harmonic kinematic (or traction) excitations of the same frequency but independent phases (and potentially different amplitudes) are applied. Such choice will lead to non-zero flux through both left and right boundaries. However, with 2 point measurements on either side of the micro-structured domain the right and left traveling waves on either side may be decomposed and the full scattering matrix can be calculated numerically.

We use the total field/ scatter field (TF/SF) formulation to more accurately measure the transmitted waves. This corresponds to the use of total field formulation in the unit cell and transmission side, and scatter formulation in reflection side of the unit cell. For more details on TF/SF formulation and the interface conditions on the incident side of the unit cell, we refer the reader to Busch et al. (2011).

We solve the TD problem by the *asynchronous Spacetime Discontinuous Galerkin* (aSDG) method (Abedi et al., 2006; Abedi et al., 2006) for elastodynamics. The simulation of the 2D problem starts from a triangular discretization of the spatial domain (unit cell and ambient zones). The *Tent Pitcher* (Abedi et al., 2004) algorithm each time *pitches* a vertex with local time coordinate in time to form a *patch* (collection) of tetrahedral elements in spacetime. The time advance of the vertices in time is limited by a special causality constraint. This results in a *patch-by-patch* solution scheme where the entire spacetime domain is gradually filled by solving one patch at a time.

The local and asynchronous solution scheme, satisfaction of balance laws at the element level, and high order of accuracy of the method in time are a few of the favorable properties of the aSDG method over other TD finite element and discontinuous Galerkin methods. In addition, low numerical dispersion and dissipation errors of the method, analyzed in Abedi and Mudaliar (2017), is of utmost importance for the parameter retrieval method; otherwise, numerical dissipation and dispersion errors accumulated over the long simulation time $[0, \overline{T}]$ would overshadow physical dispersion of the effective properties. We refer the readers to Abedi et al. (2006) and Abedi (2017) for more detailed overview of the aSDG method, and the specific formulation of the parameter retrieval method using the aSDG method.

3. 1D studies: damping vs. complex modulus

3.1. Problem description and dispersion relations

Consider the one-dimensional equation,

$$\rho \ddot{u} - C u_{,xx} = 0 \tag{14}$$

where ρ, C are homogeneous and real mass density and modulus parameters, and u is the displacement field. As discussed in Section 2.2, added loss to a unit cell can be used to choose the stable

solution branch for a lossless unit cell. In Amirkhizi (2017), loss was introduced by using complex modulus, whereas for the TD analyses to be considered herein, we introduce loss by adding a damping term to (14). In this section, we compare these two approaches for adding loss to (14). A damped version of (14) is,

$$\rho\ddot{u} + \delta\dot{u} - Cu_{,xx} = 0 \tag{15}$$

where $\delta \geqslant 0$ is the real damping coefficient.

The dispersion equations for these media are obtained by using the planar wave form introduced in Section 2.2 for displacement,

$$u(x,t) = e^{(\omega t - kx)} = e^{(\omega t - k_r x)} e^{k_i x} \tag{16}$$

in Eqs. (14) and (15). In FD, loss is often introduced by considering a complex modulus, resulting in the dispersion relation,

$$-\rho\omega^2 + (1 + \eta(\omega))k^2(\omega)C = 0 \tag{17}$$

where $\eta(\omega) := C_i(\omega)/C_r \geqslant 0$ is the ratio of imaginary to real parts of the modulus. We will first study the effect of constant η on loss characteristics and eventually propose a frequency-dependent $\eta(\omega)$ that approximates the response of (15) for low damping values. From hereon, we refer to materials and loss models corresponding to (15) and (17) as *δ-model* and *η-model*, respectively.

3.2. Loss characteristics for a slab of finite width

Once dispersion relation $k(\omega) = k_r(\omega) + k_i(\omega)$ is determined for the η- and δ-models, the loss of a slab of length l can be characterized by,

$$\mathrm{D}(l,\omega) := -k_i(\omega)l \qquad \text{dissipation exponent} \tag{18a}$$

$$a(l,\omega) := 1 - e^{-2\mathrm{D}} \approx 2\mathrm{D} \quad \text{as } \mathrm{D} \to 0 \qquad \text{absorbance} \tag{18b}$$

where a denotes how much the energy of the wave is dissipated through the nondimensional exponent D. Note that $a(l,\omega)$ matches the absorbance defined from (5) for frequency ω and a unit cell of length l in an ambient medium with the same properties.

To facilitate the discussion of the dependence of D and a on l and ω we introduce new nondimensional frequency parameters,

$$\omega_l := \frac{c_0}{l} \qquad \text{slab frequency} \tag{19a}$$

$$\omega_l' := \frac{\omega}{\omega_l} = \frac{\omega l}{c_0} \qquad \text{frequency nondimensionalized by the slab frequency} \tag{19b}$$

$$\omega_{\delta l}' := \frac{\delta l}{\rho c_0} \qquad \text{nondimensional damping for the slab} \tag{19c}$$

where $c_0 = \sqrt{C/\rho}$ is the wave speed of the lossless model (14).

Using the dispersion relation of the η- and δ-models and (18) a, we obtain,

$$\mathrm{D}(l,\omega) = \mathrm{D}(\eta,\omega_l') = \omega_l'\sqrt{\frac{\sqrt{1+\eta^2}-1}{2(1+\eta^2)}} \to \begin{cases} \frac{\eta}{2}\omega_l' & \eta \to 0 \\ \frac{1}{\sqrt{2\eta}}\omega_l'\eta \gg 1 \end{cases} \qquad \eta - \text{model} \tag{20a}$$

$$\mathrm{D}(l,\omega) = \mathrm{D}(\omega_{\delta l}',\omega_l') = \omega_l'\sqrt{\frac{\sqrt{1+\left(\frac{\omega_{\delta l}'}{\omega_l'}\right)^2}-1}{2}} \to \begin{cases} \frac{\omega_{\delta l}'}{2}\omega_{\delta l}' \ll \omega_l' \\ \sqrt{\frac{\omega_{\delta l}'\omega_l'}{2}} \quad \omega_{\delta l}' \gg \omega_l' \end{cases} \qquad \delta - \text{model} \tag{20b}$$

as evident, η and $\omega_{\delta l}'$ control loss response of the η- and δ-models, respectively.

Fig. 3 compares the energy loss of the two model versus frequency in terms of a for the simple problem of a single layer 1D unit cell, embedded by the same ambient material. This form is preferable over D for the analysis of the effect of added loss in the parameter retrieval method. In (20) a, for the η-model D is linearly proportional to ω_l' whereas in (20) b D is almost independent from ω_l' when $\omega_{\delta l}' \ll \omega_l'$. This explains rather linear dependence or constant value of a for low ω_l' in Fig. 3(b) for the η- and δ-models, respectively. The deviation of loss from $\omega_{\delta l}'/2$ and its limit to zero in Fig. 3(b) as $\omega_l' \to 0$ corresponds to the solution branch $\omega_{\delta l}' \gg \omega_l'$ in (20) b, wherein D is simultaneously proportional to $\sqrt{\omega_{\delta l}'}$ and $\sqrt{\omega_l'}$. Finally, it is noted that for low loss parameters D, hence a, scale linearly versus η and $\omega_{\delta l}'$ for the η- and δ-models, respectively. This would facilitate successive reduction of the loss parameter to reduce overall absorption below certain limit when attempting to retrieve the parameters of a lossless unit cell.

Next, the discrepancy of the retrieved material parameters of the lossy models is investigated with respect to those of the lossless model in (15). For both models the real parts of the constitutive parameters exactly match those of the lossless medium. For the δ-model, C_i is exactly retrieved to be zero. However, clearly the retrieved imaginary modulus is $C_i = \eta C_r$ for the η-model. For the mass density, ρ_r is exactly zero for the η-model. In contrast, $\rho_r = -\delta/\omega\rho$ for the δ-model. This error tends to infinity as frequency tends to zero.

By comparing the previous results, it is concluded that the δ-model is preferred from energy perspectives in that a rather uniform energy loss is introduced across all frequencies. However, in terms of retrieved constitutive material parameters, the accuracy of this scheme reduces at low frequencies. Given that η- and δ-models are more naturally incorporated into FD and TD methods, this observation suggests that a FD method and complex modulus loss may be preferred for low frequencies. Similarly nonzero damping appears to be appropriate for a TD method at higher frequencies. Interestingly, even from computational cost analysis of the two methods, a TD method is preferable over a FD one, for the retrieval of material properties at higher frequencies. This could be the motivation of a hybrid FD-TD scheme, with added appropriate loss, to characterize lossless unit cells over a wide range of frequencies. Finally, it is noted that an η-model where $\eta(\omega) \propto 1/\omega$ is employed in Section 5.4 to resemble a δ-model with low damping values.

4. 1D unit cells: Use of loss in parameter retrieval method

We consider three different 1D multilayer unit cells. The two loss models are first compared through the solution of a three-layer unit cell in Section 4.1. Next, two variants of a five-layer unit cell are presented in Sections 4.2 and 4.3. In the former example, pass-bands and stop-bands of the unit cell and the form of dispersive properties within each band are discussed. In the latter example, added loss is used to decide between double positive and double negative solutions for the second pass-band of the lossless unit cell. It is noted that for all these examples, the scattering parameters are analytically derived from (4).

For lossy unit cells, one of the loss models is used for some or all layers of the unit cell. When the η-model is used, η is specified for some or all of the layers. For the δ-model, the absolute value of damping δ, rather than $\omega_{\delta l}' = \delta l/\rho c_0$, is used. The reason is that for a multilayer unit cell, it is not clear what mass density and wave speeds should be used, due to the existence of multiple layers and the fact the effective mass density and wave speed are often dispersive.

The geometry of the unit cell is specified by $[l] = [l_1, \ldots, l_m]$, where as in Section 2.1, m is the number of layers and l_1 to l_m

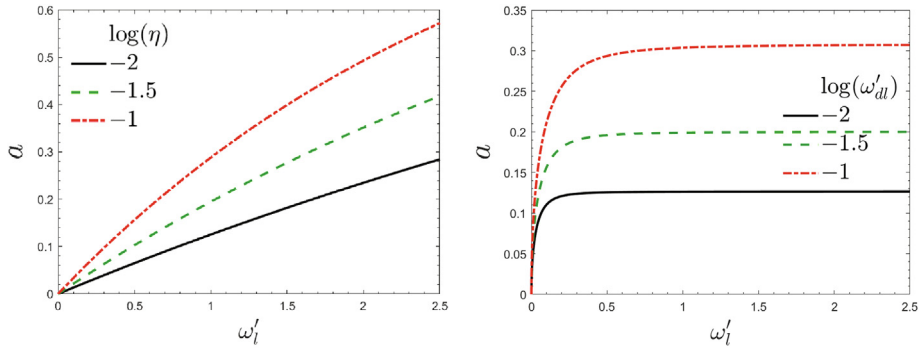

(a) η-model. (b) δ-model.

Fig. 3. The added energy loss for the slab of length l through two different loss mechanisms for a range of frequencies.

are the lengths of individual layers. The moduli and mass densities of the layers are similarly represented by $[C] = [C_1, \ldots, C_m]$ and $[\rho] = [\rho_1, \ldots, \rho_m]$, respectively. These values are real unless a complex modulus is chosen for certain layers in η-model. Similarly, for the δ-model, nonzero damping can be considered for some layers. Finally, we use the unit system $[\text{mm}, \mu\text{s}, \text{mg}]$ for length, time, and mass. This results in the $[\text{km/s}, \text{GPa}, \text{g/cm}^3, \text{M rad / s}, \text{MHz}, \text{MRayl}, \text{g/cm}^3\mu\text{s}]$ units for velocity, stress, density, angular frequency, frequency, impedance, and damping coefficient.

4.1. Three-layer slab

The three-layer example in this section is taken from Nemat-Nasser et al. (2011) and Amirkhizi (2017). The material properties and geometry of the problem are as follows: $[C] = [8.68, 320, 8.68]$, $[\rho] = [1.18, 7.954, 1.18]$, and $[l] = [1.5, 0.8, 1.5]$. The ambient medium properties are modulus $C_0 = 10.2424$ and $\rho_0 = 1$. Thus, the impedance of the ambient material matches that of the outer layers of the unit cell. In the following loss is only added to the outer layers of the unit cell, that is for layers one and three, to enable unambiguous determination of the properties of the lossless unit cell.

Fig. 4 shows some of the (intermediate) parameters of the parameter retrieval method. From (10), retrieved k and Z are used to compute C and ρ. We focus on k as its derivation involves the determination of integer p in (9). Fig. 4(a) shows k_i whose value does not involve p. In Fig. 4(b), $\phi = \pi$ for $\omega \in [1.24, 2.82]$. This is a stop-band wherein $k_i < 0$.

At the start of the stop band, the k solutions associated with $\phi = \pi$ and $\phi = -\pi + 2p\pi$ with $p = 1$ coincide, since $k_i = 0$ for the lossless system. Furthermore, Z solutions associated with positive and negative branches $\phi = \pm\pi + 2p\pi$ are discontinuous at this point. Therefore, continuity considerations (for Z) fail to determine the branch at the beginning of the stop band for the lossless system. In fact, both selection will again coincide at the end of the stop band, through which ϕ values do not change, and upon its end Z values vanish (see Fig. 5) as well as k_i values. In other words, due to the behavior (poles and zeros) of the apparent impedance and multi-valued nature of phase advance, it is not possible to determine these quantities as unique functions of frequency in idealized lossless systems. See Amirkhizi (2017). Furthermore, at $\omega = 2.82^+$ ϕ can either increase above or decrease below π. For a lossless unit cell, both options are valid since $k_i = 0$ for $\omega \in [2.82, 3.36]$. In this range, $\phi/2\pi$ can take values in $[1/2, 1]$ or $[0, 1/2]$. In summary, if one only considers lossless systems, continuity considerations are insufficient to remove branch ambiguity both at the beginning and ending of the stop bands.

In such case, however, the solutions of the lossy unit cells help determine the stable branch; see Amirkhizi (2017). As shown Fig. 4 (a), $k_i < 0$ for $\omega \in [2.82, 3.36]$ and only the branch $\phi/2\pi \in [0.5, 1]$ is valid since $\phi/2\pi = 1/2$ or $-1/2 + p$ (where p = 1) can only occur when k_i is non-zero and different for the two branches; this facilitates choosing the stable branch for the lossless unit cell. Since there is a discontinuity of θ at $\phi = \pi$ in the log operation in (9), to maintain the continuity of ϕ, p jumps from zero to one in Fig. 4(c) when ϕ exceeds π in Fig. 4(b). As δ increases, the frequency for this transition transitions from 2.82 to 1.24. Finally, C_r is shown in Fig. 4(d). As evident, added loss regularizes the sharp corners of C_r and k spectra of the lossless unit cell. The use of loss in choosing the stable solution branch is described more thoroughly through the example in Section 4.3.

Fig. 6 shows the retrieved modulus and mass density parameters. As $\omega \to 0$, mass density tends to the quasi-static limit $\rho = 2.60$ which is the volumetric average of individual layer densities. The quasi-static limit of modulus is $C = 10.92$, which corresponds to the compliance obtained by the volumetric average of compliance values of individual layers. Infinite and zero values of C and ρ correspond to frequencies $\omega = 1.24, 2.82, 3.36$. As evident, the retrieved constitutive parameters for lossy unit cells smoothen those of the lossless unit cell around these frequencies. In addition, similar to the single-layer analysis in Section 3, we observe that the error in retrieved ρ_r grows as $\omega \to 0$ in Fig. 6(b) when using the δ-model.

To compare the two loss models, two retrieved parameters are shown in Fig. 7. The retrieved constitutive parameters are very similar for the two models in that they are more heavily regularized near the boundaries of the stop-band, as shown for ρ_r in Fig. 7(a). More interesting observation is for a in Fig. 7(b). From the single-layer analysis in Section 3.2, we observed that the energy loss increases versus frequency for the η-model, whereas it stayed relatively constant for the δ-model. For this more complex unit cell, while there are some similarities on how a is higher for the δ-model at low frequencies, overall there is no clear resemblance to the solutions of a single-layer unit cell. For example, a varies considerably for the δ-model. In terms of the effectiveness of the two loss models, very similar solutions are obtained in Figs. 6 and 7(a). Thus, this example suggests that if the loss value is judiciously chosen for either model and the limit of the retrieved solutions is taken when the loss tends to zero, one can unambiguously find the sable branches of solution for a lossless unit cell.

4.2. Five-layer slab A

In Nemat-Nasser and Srivastava (2011) a five-layer 1D unit cell is considered with the formation $P_1P_2P_3P_2P_1$, where P_1, P_2, and P_3

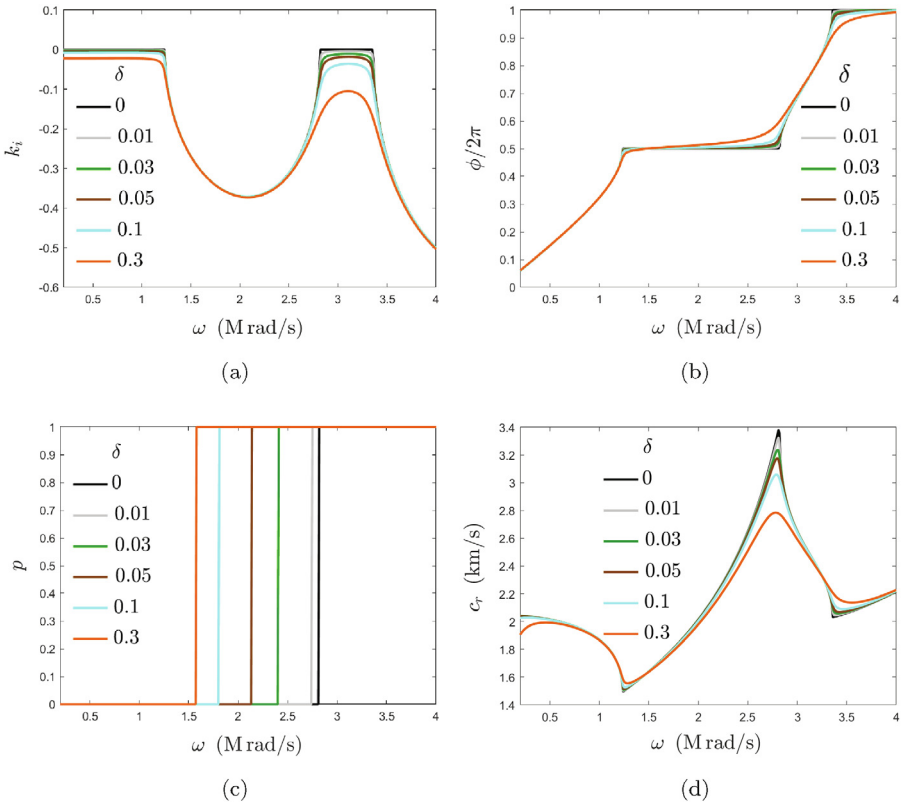

Fig. 4. Quantities needed in the parameter retrieval method for choosing the right solution branch for the 3-layer unit cell.

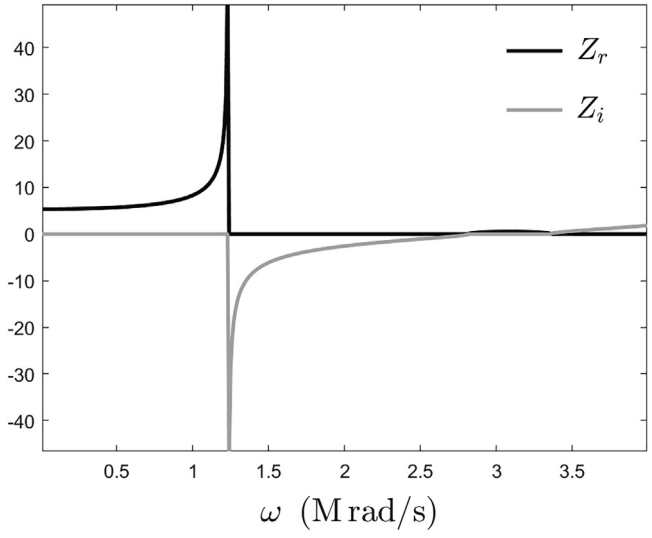

Fig. 5. Retrieved impedance for the lossless 3-layer unit cell.

are the phases of material in the unit cell and subscripts 1, 2, 3 are used to decorate properties of each of these phases. The mid-layer is a material of high density $\rho_3 = 8$ and modulus $C_3 = 320$. Material properties of the outside layers P_1 are $\rho_1 = 1.18$ and $C_1 = 8.7$. The density of P_2 is $\rho_2 = 1.1$, whereas its modulus, C_2, takes four different values. The thicknesses of these layers are $l_1 = 1.45, l_2 = 0.5$, and $l_3 = 0.435$. Thus, the material and geometry properties of the unit cell are: $[C] = [8.7, C_2, 320, C_2, 8.7], [\rho] = [1.18, 1.1, 8, 1.1, 1.18]$, and $[l] = [1.45, 0.5, 0.435, 0.5, 1.45]$.

The response of this unit cell is highly sensitive to the density of P_3 and compliance of P_2 and much less on the length and properties of P_1. As the mismatch between the moduli of P_2 and P_3 increases, the first and second pass-band and stop-bands move to lower frequencies and for higher values of mismatch even double negative properties are reported over a fraction of the second pass-band, whose width increases with increasing compliance of P_2. The configuration A, denoted by 5LA, has the lowest mismatch of the moduli of P_2 and P_3 by having $C_2 = 2.2$, whereas the highest mismatch is achieved in configuration *D*, denoted by 5LD, with $C_2 = 0.02$.

By using a higher modulus $C_2 = 2.2$ for the 5LA unit cell, the stop-band and pass-bands are more evenly spread. This facilitates the discussion on the solution features within each frequency band in this section. In section Section 4.3, the most extreme configuration, 5LD, is considered to investigate the possibility of achieving double negative properties in the second pass-band. For both cases the properties of the ambient layers in parameter retrieval method are $C_0 = 10$ and $\rho_0 = 1$. For solutions that a lossy unit cell is considered, loss in the form of nonzero damping or imaginary modulus, is only considered in P_2. That is, the modulus and damping of P_2 are $(1 + \eta)C_2$ and δ, respectively. Clearly, for the lossless unit cells, η and δ are zero for all phases, including P_2.

We first consider the lossless 5LA unit cell. For this unit cell, there are two types of stop-bands. For the first type, phase angle ϕ remains equal to $2\pi(p + 0.5)$, where p is the number of full wave cycles within a unit cell with equivalent properties and also the number of stop-band of this kind. The start and end frequencies for this stop-band are denoted by $\omega_{p+0.5^l}$ and $\omega_{p+0.5^r}$, respectively. These are called *half-cycle* stop-bands and are denoted by the red color. For the second type of stop-band, the phase angle ϕ remains equal to $2\pi(p + 1)$, where $p + 1$ is the number of full wave cycles in the unit cell with equivalent properties and p is the number of such kind of stop-bands; e.g. in many cases for p = 1 is the first full cycle stop band but the second stop band after a half cycle stop band at

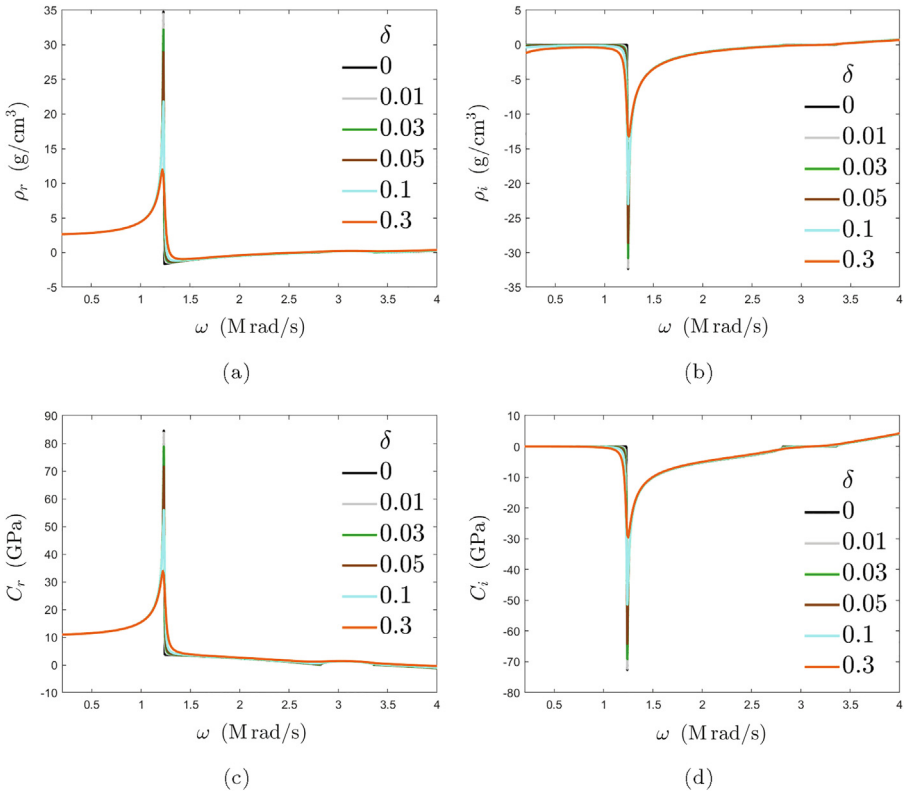

Fig. 6. Retrieved constitutive parameters for the 3-layer unit cell.

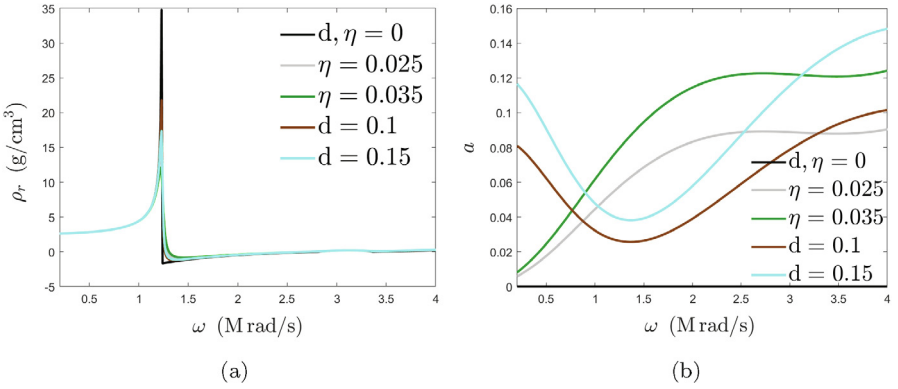

Fig. 7. Comparison of the two loss models for the retrieved constitutive parameters and absorbance.

lower frequencies. The frequencies for the start and end of these stop-bands are denoted by ω_{p+1^l} and ω_{p+1^r}, respectively. These are called *full-cycle* stop-bands and are denoted by blue.

In all plots in this section and Section 4.3, the boundaries of half- and full-cycle stop-bands are shown by red and blue lines, respectively. Dot-dash and dash lines denote the start and end of the stop-bands. The regions between blue and red lines are the pass-bands. Table 1 lists the frequencies of the stop-bands for the first two cycles of the 5LA unit cell. Since retrieved properties in (10) depend on Z and k, we first study the form of these fields in stop-bands and pass-bands.

Fig. 8 shows parameters n and d needed to determine Z from (8) a. For half-cycle stop-bands the start frequency $\omega_{p+0.5^l}$ corresponds to $d = 0$ and for $\omega_{p+0.5^r}$ we have $n = 0$. This is reversed for full-cycle stop-bands in that $n = 0$ and $d = 0$ at the start ω_{p+1^l} and end ω_{p+1^r} of the stop-band, respectively. As a result, at the boundaries of pass-bands between half and full cycles $n = 0$ and at the boundaries of pass-bands between full and half cycles $d = 0$. These aspects can be observed in Fig. 8(a). While both n and d are complex, as shown in Fig. 8(b), the ratio n/d remains real for this lossless unit cell.

Table 1
End points of the stop-bands for the 5LA unit cell. The frequencies are accurate to within 0.0025.

Cycle number p	$\omega_{p+0.5^l}$	$\omega_{p+0.5^r}$	ω_{p+1^l}	ω_{p+1^r}
0	1.0850	1.3825	1.9700	3.3175
1	3.5150	5.5200	5.6375	7.4575

Given that from (8) a, $Z = Z_0\sqrt{\frac{n}{d}}$, and that n/d is real in (8(b)), Z is real when $n/d \geqslant 0$ and imaginary when $n/d < 0$. In addition,

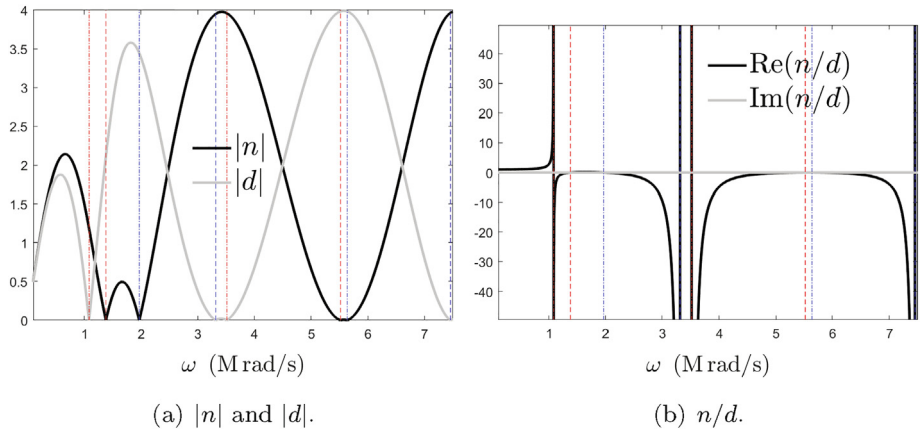

Fig. 8. The parameters n and d needed to determine Z from (8) a for the 5LA unit cell.

from Fig. 8(a), $Z = 0$ at the end of half-cycle and start of full-cycle stop-bands, *i.e.,* when $n = 0$. Moreover, $|Z| \to \infty$, at the start of half-cycle and end of full-cycle stop-bands, that is when $d \to 0$; for the side that $d \to 0^+, Z_r \to \infty$ and $Z_i = 0$, while for $d \to 0^-, Z_r = 0$ and $Z_i \to \pm\infty$. These aspects can be observed in Fig. 9.

Next, the form of k is studied through ζ. From (7), $|\zeta| = e^{-k_i l}$ and $k_r l = \theta + 2p\pi$; *cf.* (9). Since $k_r \leqslant 0, |z| \geqslant 1$. Thus, $1/\zeta$ is more suitable for the analysis in this section given that its absolute value remains bounded by 1. Fig. 10 shows the real, imaginary, and absolute value of $1/\zeta$ as a function of ω. As shown, $|\zeta| = 1$ and $|\zeta| > 1$, in pass-bands and stop-bands, respectively.

The form of $1/\zeta$ in stop-bands and pass-bands can more clearly be observed in Fig. 11, where the curve of $1/\zeta$ with argument $\omega \in [0, \omega_{2^r}]$ is shown in the complex plane. In the first pass-band for $\omega \in [0, \omega_{0.5^l}], |\zeta| = 1$ and its argument increases to π. This is demonstrated by unit value of $1/\zeta$ and decrease of its argument from 0 to $-\pi$ in Fig. 11(a). For the first half-cycle pass-band, $|\zeta| = 1$ at $\omega_{0.5^l}$, the beginning of the band. From Fig. 10, through this stop-band $1/\zeta$ is real and negative; it starts with value -1 at $\omega_{0.5^l}$, increases above -1, and recovers the value -1 at $\omega_{0.5^r}$. Thus, the phase of $1/\zeta$ is $-\pi$ and its amplitude decrease and then recover back to 1 during this stop-band as shown in Fig. 11(b). For the second pass-band between $\omega_{0.5^r}$ and $\omega_{1^l}, |\zeta| = 1$ and ϕ increases from π to 2π; *cf.* Fig. 10. This corresponds to the unit value of $1/\zeta$ and decrease of its argument from $-\pi$ to -2π in Fig. 11(c). Finally, as shown in Fig. 10, for the first full-cycle stop-band $\omega \in [\omega_{1^l}, \omega_{1^r}], 1/\zeta$ is real and positive, taking the value one at ω_{1^l} and ω_{1^r} and smaller than one in between. This corresponds to constant argument of -2π and decrease and then increase of magnitude of $1/\zeta$ in Fig. 11(d).

In Fig. 11, the green lines show the connection from the last line of a pass-band to a stop-band and vice versa and are a result of discrete sampling of frequencies (3000 points with step size of 0.0025 for this problem). The complex plane plots for $1/\zeta$ are useful to examine the sufficiency of sampled frequencies to find the boundaries of the stop-bands. In short, for this lossless unit cell, $|\zeta| = 1$ in pass-bands and it increases beyond one in half- and full-cycle stop-bands for which the argument for ζ is π and zero, respectively. The corresponding phase angle $\phi = k_r l$ is shown in Fig. 12(a), where p increases at the end of half-cycle stop-bands to accommodate continuity of $\phi = \arg(\zeta)$. As will be shown in Section 4.3, with the assumption of continuity of k in ω (or ϕ in ω), a necessary but not sufficient condition to realize double negative properties is for ϕ to decrease, rather than increase, at the end of (the first) stop-band. Finally, k is shown in Fig. 12, where $k_r = \phi/l$ and $k_i = -\log(|\zeta|)/l$; *cf.* (9). As implied by their names, in stop-bands

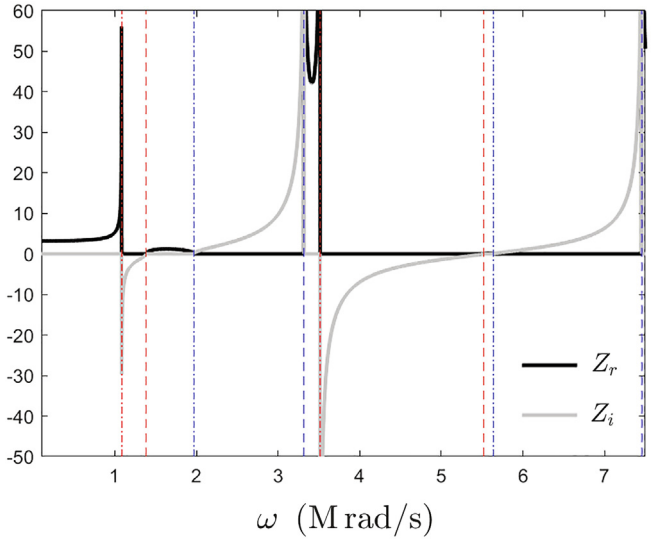

Fig. 9. The retrieved Z from (8) a for the 5LA unit cell.

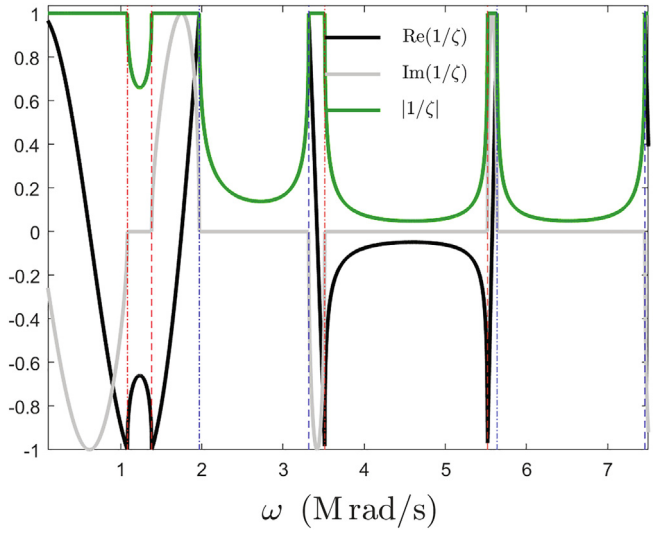

Fig. 10. The parameter $1/\zeta$ needed to determine k for the 5LA unit cell.

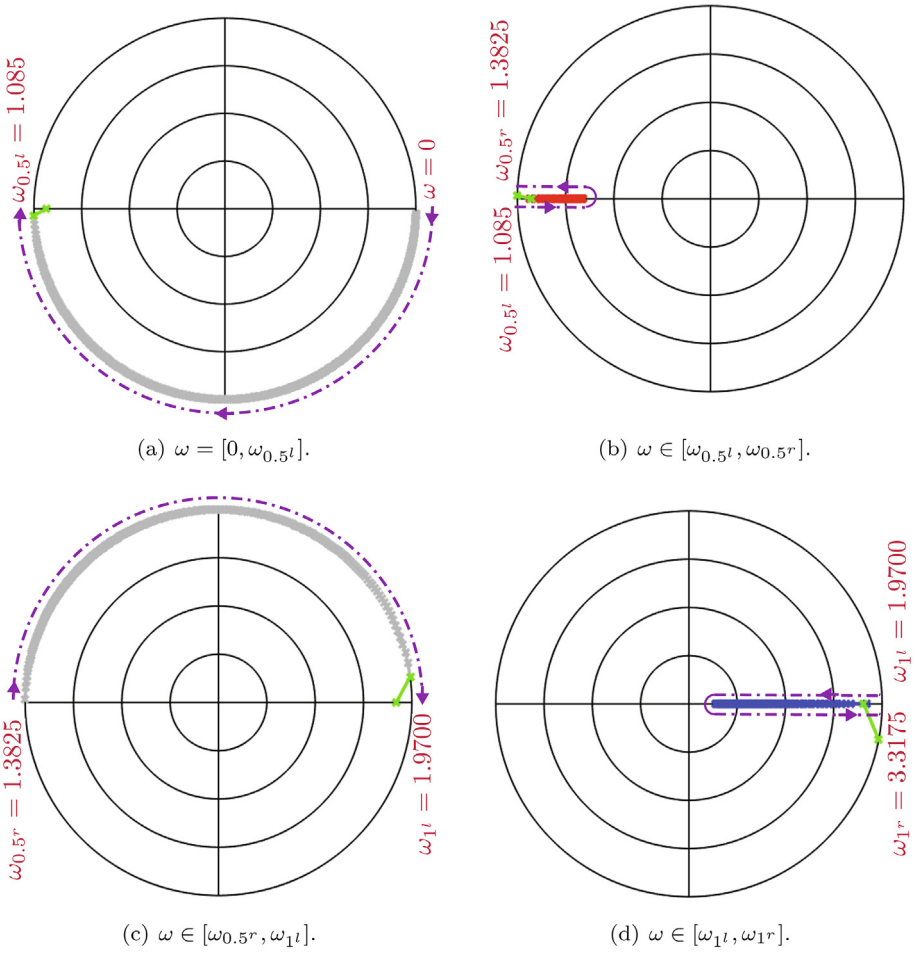

(a) $\omega = [0, \omega_{0.5^l}]$. (b) $\omega \in [\omega_{0.5^l}, \omega_{0.5^r}]$.

(c) $\omega \in [\omega_{0.5^r}, \omega_{1^l}]$. (d) $\omega \in [\omega_{1^l}, \omega_{1^r}]$.

Fig. 11. The phase space of $1/\zeta$ at the end of pass-bands and stop-bands for $\phi = \pi_-, \pi_+, 2\pi_-, 2\pi_+$. The red and blue segments on negative and positive real axes, correspond to half- and full-cycle stop-bands, respectively. Arrows on the purple dotted-dashed line show the direction at which ω increases. (For interpretation of the references to colour in this figure legend, the reader is referred to the web version of this article.)

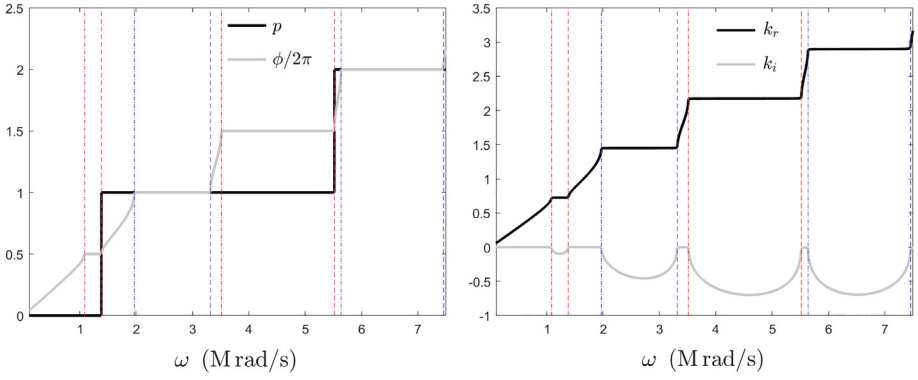

(a) p and ϕ versus ω. (b) Retrieved k from (9).

Fig. 12. Quantities needed in (9) for choosing the right solution for ϕ and k for the 5LA unit cell.

$k_i < 0$ implying an evanescent propagation mode; in contrast in pass-bands $k_i = 0$.

The retrieved material properties for the lossless 5LA unit cell are shown in Fig. 13. Since k is the same at the end points of stop-bands, C_r increases in stop-bands in Fig. 13(a). Retrieved mass density is shown in Fig. 13(b). In the first pass-band $Z_i = 0$ and as $\omega \to \omega_{0.5^l}, Z_r \to \infty$; *cf.* Fig. 9. As a result, ρ is real and tends to infinity as $\omega \to \omega_{0.5^l}$; *cf.* (10). In the first half-cycle stop-band $Z_r = 0$ and $\rho_r = Z_i k_r/\omega$; since $Z_i \to -\infty$ and $Z_i \to 0$ as $\omega \to \omega_{0.5^l}$ and $\omega \to \omega_{0.5^r}$, respectively, and k_r is constant, ρ_r tends to $-\infty$ at the start of this stop-band and reaches zero at $\omega_{0.5^r}$. The negative k_i tends to zero with the same rate at which Z_i tends to $-\infty$ as $\omega \to \omega_{0.5^l}$ in this stop-band; since $\rho_r = -Z_i k_i/\omega, \rho_r$ takes a negative finite value and zero at $\omega_{0.5^l}$ and $\omega_{0.5^r}$, respectively. In the second pass-band

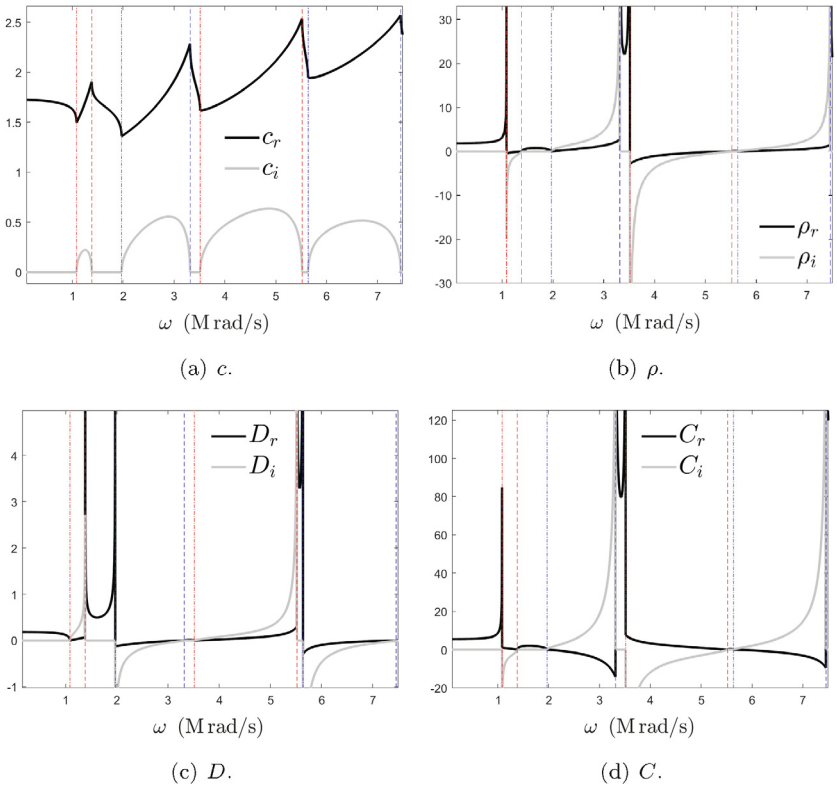

Fig. 13. Retrieved constitutive parameters for the 5LA unit cell. The boundaries of bands are defined in terms of $\phi = n\pi$, where n is an integer; *cf.* Table 1.

for $\omega \in [\omega_{0.5^r}, \omega_{1^l}]$, similar to the first pass-band $Z_i = 0$. Thus, $\rho_r = 0$ and ρ_r takes a profile similar to Z_r; that is, zero at the end points and positive in between. Finally, in the first full-cycle stop-band $Z_r = 0$ and Z_i tends to ∞ as $\omega \to \omega_{1^r}$. By an argument similar to that for the first half-cycle stop-band, we observe that $\rho_r \to \infty$ and ρ_r takes a finite positive value at $\omega \to \omega_{1^r}$, and $\rho = 0$ at ω_{1^l}. This profile of ρ repeats in the second cycle $\omega \in [\omega_{1^r}, \omega_{2^r}]$, where upon ρ starting from a positive infinite limit at ω_{1^r}, the same response of the first pass-band is observed in this band and the in next corresponding bands between the first and second cycles.

The retrieved compliance is shown in Fig. 13(c). Since $D = k/Z\omega$ and $\rho = kZ/\omega$, impedance plays a reverse role for D. That is, in the half cycle pass-bands $\left[\omega_{p+0.5^r}, \omega_{p+1^l}\right]$, real ρ and D take zero and positive infinite values at the end points, while in full cycle pass-bands $\left[\omega_{p+1^r}, \omega_{p+1.5^l}\right]$ the opposite occurs. By noting that $|Z|$ and k_i tend to zero with the same rate at $\omega_{p+0.5^r}$ and ω_{p+1^l}, finite positive and negative values for D_r are realized in stop-bands at these points, respectively. Positive and negative infinite limits are realized for D_i at these points in the stop-bands. Finally, the retrieved modulus is shown in Fig. 13(d). Since $C = Z\omega/k$ and $\rho = kZ/\omega$, retrieved $C = 1/D$ is similar to ρ; the difference is in nonzero positive and negative real values for C_r at $\omega_{p+0.5^l}$ and ω_{p+1^r}, respectively, as opposed to opposite sign values for ρ_r. This is due to the appearance of k in denominator for C.

In short, material is single negative in stop-bands; $C_r, D_r \geqslant 0$ and $\rho_r \leqslant 0$ in $\left[\omega_{p+0.5^l}, \omega_{p+0.5^r}\right]$, and $C_r, D_r \leqslant 0$ and $\rho_r \geqslant 0$ in $\left[\omega_{p+1^l}, \omega_{p+1^r}\right]$. Moreover, (ρ_r, C_r) and D_r take zero and infinite values at the limits of $\left[\omega_{p+0.5^r}, \omega_{p+1^l}\right]$ and $\left[\omega_{p+1^r}, \omega_{p+1.5^l}\right]$ pass-bands, respectively. Material is double-positive in the pass-bands with zero imaginary properties. The possibility of a double negative material in pass-bands of these five-layer unit cells is discussed in Section 4.3.

The effect of added loss is studied in subsequent figures. As shown in Figs. 13(d) and 14(b), for lossy unit cells $|n|$ and $|d|$ no longer become zero (at the boundaries of stop-bands of the lossless unit cell). As a result, $|Z|$ does not tend to zero or infinity at any frequencies. The real and imaginary parts of Z are shown in Fig. 14(b) and (d).

Added loss has a similar smoothing effect on ζ; see Fig. 15(a); as a result retrieved ϕ, k_i, and c in Fig. 15(b–d) are smoothened out at the sharp corners by the added loss. Fig. 16 shows ρ as one of the retrieved constitutive parameters. Since $|Z|$ no longer takes zero and infinite values through the introduction of loss, retrieved properties such as ρ no longer tend to infinity and are continuous. The difference between the retrieved C_r and ρ_r in Figs. 15(d) and 16(b) for lossy and lossless unit cells is relatively large as $\omega \to 0$. This is consistent with the analysis in Section 3. Finally, it is noted that as higher values of loss are introduced some solution features are lost. For example, in Figs. 15(d) and 16(b) and Fig. 16(a), retrieved Z_r and ρ_r are convex rather than concave in $[\omega_{1^r}, \omega_{1.5^l}]$ for $\delta = 1$.

4.3. Five-layer slab D

The 5LD unit cell has the smallest modulus value of $C_2 = 0.02$ in P_2 among the four unit cells considered in Nemat-Nasser and Srivastava (2011). Table 2 lists the start and end frequencies of half-cycle and full-cycle stop-bands for four complete cycles. In comparison to Table 1, it is observed that lowering C_2 shifts all end points of stop-bands to lower frequencies and significantly shrinks half-cycle stop-bands. Fig. 17 shows retrieved properties up to the second pass-band for the lossless 5LD unit cell, where both ρ_r and D_r are negative. These retrieved *double negative* (DN) properties are reported in Nemat-Nasser and Srivastava (2011). Below, we will demonstrate that while these solutions are consis-

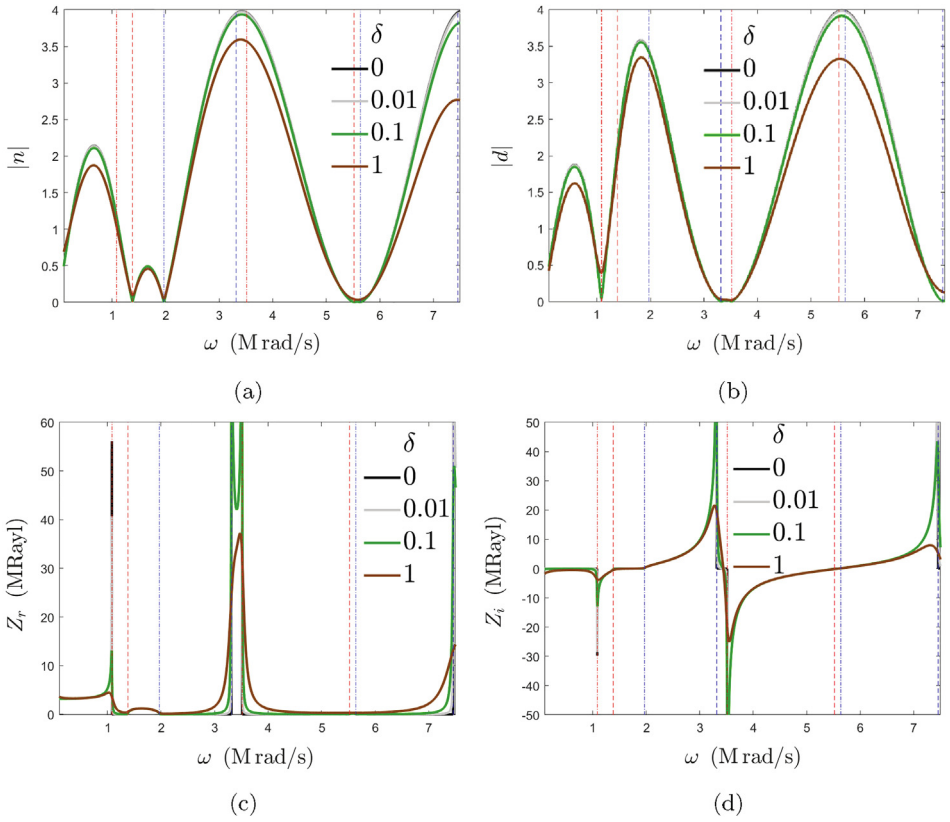

Fig. 14. The departure of parameters n and d from zero, and continuity and nonzero value of Z as loss is added to the 5LA unit cell.

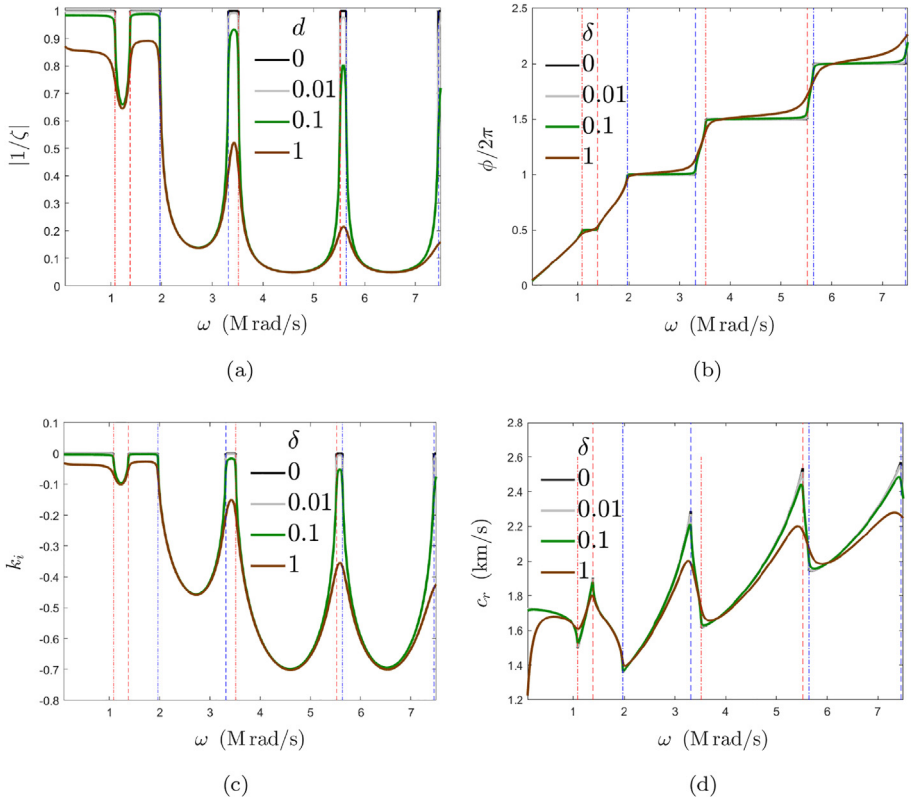

Fig. 15. The effect of loss on the phase angle ϕ and consequently on k and c for the 5LA unit cell.

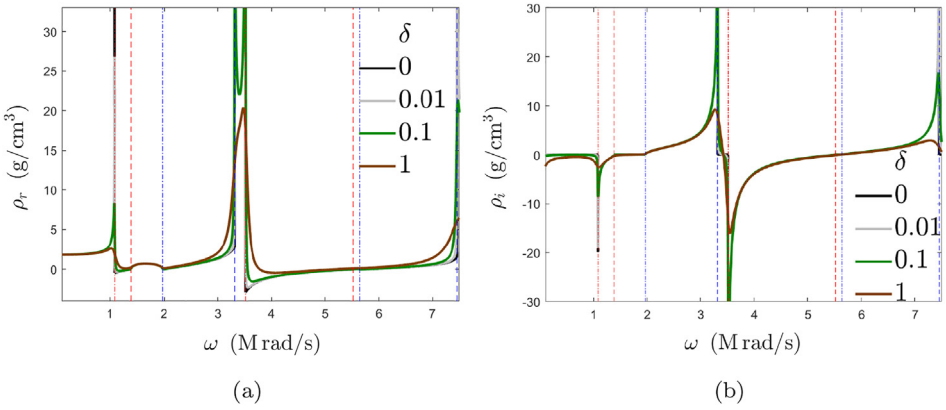

Fig. 16. The effect of loss on the retrieved density for the 5LA unit cell.

tent with the band structure of this unit cell, by adding damping to the unit cell, a double positive solution is found as the stable solution, in the sense of the definition introduced in Section 2.2, *i.e.*, that addition of an infinitesimal loss does not discontinuously change the constitutive description. Furthermore, the overall constitutive functions presented here, by construction, also reproduce the scattering response of the micro-structured medium as well as its band structure.

To investigate possible solutions in the second pass-band, $I_w := [\omega_{0.5^r}, \omega_{1^l}] = [0.145025,\ 0.209575]$, and change in the branches of the solution, we consider three alternative solutions for $\omega \in [0, \omega_{1^l}]$. These solutions are: 1) $p = 0$ with the positive root of Z, that is the root for which $Z_r \geqslant 0$, *cf.* (8) a; 2) $p = 1$ with positive root for Z_r; 3) $p = 0$ and the negative root for Z, that is the root for which $Z_r \leqslant 0$. These solutions, $+, p = 0, +, p = 1$, and $-, p = 0$ are shown by colors black, gray, and green in the following figures. As described in Section 2.2, the transformation $Z \to -Z$ results in $\zeta \to 1/\zeta$. By inspecting (9), one observes that if in addition $-p$ and p are chosen as the cycle numbers for $-Z$ and Z, we have $k \to -k$. Thus, from (10) all retrieved material properties will be unchanged by the transformation $Z \to -Z$ and $p \to -p$; the positive and negative solutions generally correspond to forward and backward propagating waves. Now, clearly $-, p = 0$ and $+, p = 0$ have such relation and they result in opposite signs for Z and k and equal signs for retrieved parameters ρ, D, and C in subsequent discussions, unless otherwise noted. As for $+, p = 0$ and $+, p = 1$, and in general any p for positive Z solutions, Z and k_i do not change and only k_r depends on p through $\phi = \theta + 2p\pi$; *cf.* (9).

Table 2
End points of the stop-bands for the 5LD unit cell. The frequencies are accurate to within 0.000025.

Cycle number p	$\omega_{p+0.5^l}$ — · — ·	$\omega_{p+0.5^r}$ — — — —	ω_{p+1^l} — · — ·	ω_{p+1^r} — — — —
0	0.143575	0.145025	0.209575	0.841175
1	0.867425	0.871975	0.896775	1.678800
2	1.692200	1.704100	1.717375	2.491275
3	2.499575	2.544275	2.553300	2.947275

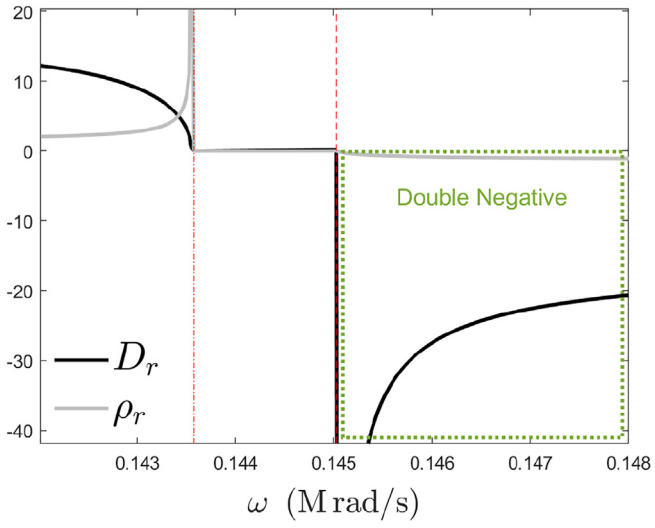

Fig. 17. Possible double negative (DN) material in the second pass-band $I_w := [\omega_{0.5^r}, \omega_{1^l}] = [0.145025,\ 0.209575]$.

The solutions for ϕ and k_i are shown in Fig. 18 from a frequency range expanded beyond $[\omega_{0.5^r}, \omega_{1^l}]$. In Fig. 18(a), for $+, p = 0, \phi$ grows from zero to π up to the beginning of the first half-cycle stop-band at $\omega_{0.5^l}$; phase angle takes the opposite value and a cycle (2π) larger value for $-, p = 0$ and $+, p = 1$ branches, respectively. The stable solution branch in this pass-band is $+, p = 0$ (for a forward moving wave). As shown in Fig. 18(b), $k_i = 0$ in this range. In the first half-cycle stop-band $[\omega_{0.5^l}, \omega_{0.5^r}]$, phase angle does not change for any of the solution branches considered. That is, for $+, p = 0$ and $+, p = 1$, $\phi = \pi$ and 3π, respectively. For both solutions, k_i becomes negative and goes back to zero from the start to the end of the stop-band, as shown in Fig. 18(b). Opposite sign k (and ϕ) for $-, p = 0$ and $+, p = 0$ would result in $\phi = -\pi$ and positive k_i for the $-, p = 0$ solution branch in this stop-band. However, for forward-moving waves considered, this solution is not acceptable since k_i becomes positive. As will be shown later, *cf.* Fig. 20(c), $Z_r = 0$ in this stop-band and both positive and negative solutions would coincide by requiring $k_i \leqslant 0$. Thus, to preserve the continuity of k, solution stays in the $+, p = 0$ branch in this stop-band. Note that branch $-, p = 1$ (not shown) is also available as k is continuous at the boundaries of the stop band and that Z being discontinuous and vanishing at the left and right ends, respectively, does not preclude it. However, by definition adopted earlier, it is not a forward moving wave and is not considered. Note that as discussed further, the "stability" criterion is not hindered by any such challenges.

In the pass-band $I_w = [\omega_{0.5^r}, \omega_{1^l}]$, as will be discussed both $+, p = 1$ and $-, p = 0$ are valid solution branches. In the onset of this pass-band, ϕ jumps to $-\pi$ for $+, p = 0$. Phase for $+, p = 1$ drops to π. Thus, this branch result in a continuous increase of ϕ from π for $+, 1$ branch at $\omega_{0.5^r}$ to 2π at ω_{1^l}. The solution branch $-, p = 0$ has the opposite ϕ of $+, p = 0$ in this pass-band and ϕ jumps ini-

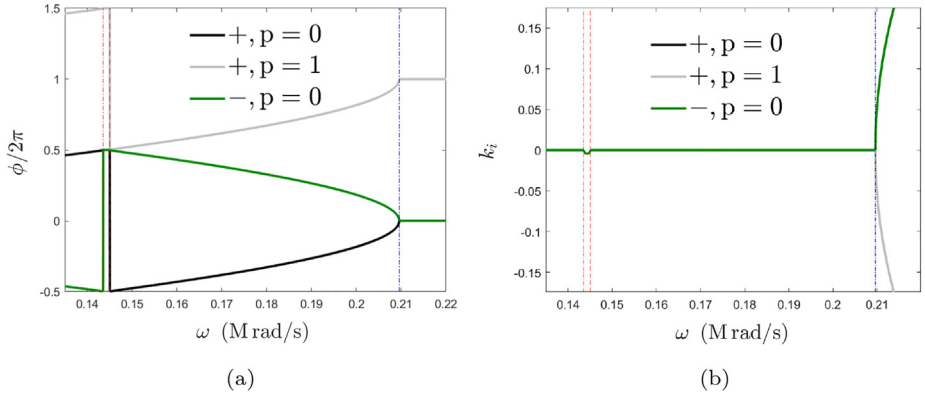

Fig. 18. Phase angle ϕ and k_i for the three branches of solution for the 5LD unit cell.

tially from $-\pi$ to π. Thus, this branch too can be an alternative continuous extension of ϕ from that of $+, p = 0$ beyond ω_{0^r}. Since $k_i = 0$ for both $+, p = 1$ and $-, p = 0$ branches, both solutions are valid and have no loss in this pass-band. The difference is that for $+, p = 1$, ϕ increases to 2π while for $-, p = 0$ it decreases to 0 in I_w. Next, we will compare the other retrieved parameters for $+, p = 1$ and $-, p = 0$ in I_w.

The real part of the retrieved material properties for these three solution branches are shown in Fig. 19. It is noted that since in $I_w, k_i = 0$ (Fig. 18)(b) and $Z_i = 0$ (not shown), all retrieved material properties are real. We will compare the solutions for $+, p = 1$ and $-, p = 0$ branches in I_w. While C_r does not considerably change for $+, p = 1$ in Fig. 19(a), it tends to infinity for the $-, p = 0$ branch. This is due to the fact that $k = k_r = \phi/l$ decreases to zero as $\omega \to \omega_{1^l}$ for $-, p = 0$; *cf.* Fig. 18(a). As mentioned before, positive and negative branches correspond to positive and negative Z_r (when $Z_r \neq 0$). This can be observed in positive and negative values for Z_r for $+, p = 1$ and $-, p = 0$ in Fig. 19(b). As shown in Fig. 19(b) and (d), positive and negative D_r and ρ_r are retrieved for $+, p = 1$ and $-, p = 0$ branches. This is expected, given that $k = k_r > 0$ and Z_r is positive and negative for $+, p = 1$ and $-, p = 0$ branches; *cf.* (10). In short, both double positive and double negative solutions corresponding to $+, p = 1$ and $-, p = 0$ are valid in I_w.

By introducing loss to the unit cell, between the $+, p = 1$ and $-, p = 0$ branches, one takes a positive and one takes a negative k_i in $[\omega_{0.5^r}, \omega_{1^l}]$. For the lossless unit cell, while both branches are valid, the branch that corresponds to negative k_i for lossy unit cells is the stable branch, as discussed in Section 2.2. The solutions for lossy unit cells, with low, intermediate, and high damping and complex modulus ratio values (in P_2) are shown in Fig. 20. The negative values of k_i for $\omega \in I_w$ in Fig. 20(a), in fact, correspond to the $+, p = 1$ branch. As shown in Fig. 20(b), by increasing loss the frequency at which the switch from $+, p = 0$ to $+, p = 1$ occurs shifts from the right of the stop-band at $\omega_{0.5^r}$ to roughly its center. The

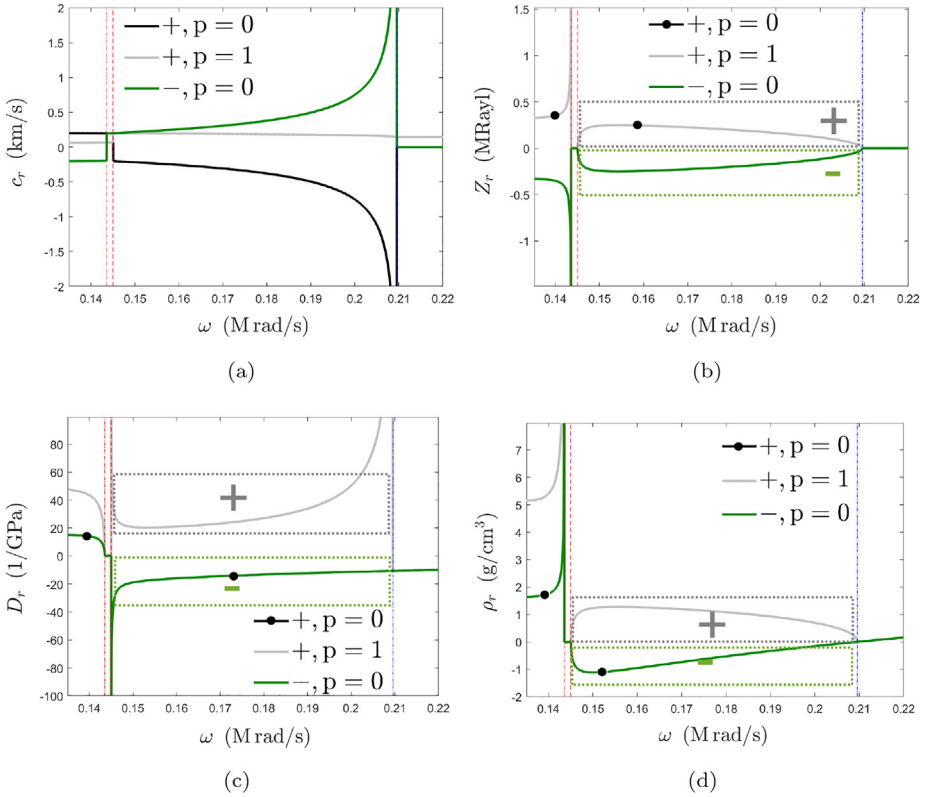

Fig. 19. Retrieved properties for the three branches of solution for the 5LD unit cell.

choice of $+, p = 1$ solution branch manifests itself in positive values for Z_r, ρ_r, D_r, and C_r in I_w in Fig. 20(c–f). Thus, $+, p = 1$ and double-positive solutions in Figs. 18 and 19 are the stable solutions in I_w. A few other arguments, based on the continuity retrieved parameters, are provided in Appendix A on why $+, p = 1$ is the stable solution branch in I_w. Taking the $+, p = 1$ solution branch in the second pass-band, the double-positive retrieved parameters for the lossless unit cell are shown in Fig. 21.

Fig. 22 shows k for four full cycles of wave. The high contrast ratio of the moduli between P_3 and P_2 results in extremely narrowed half-cycle stop-bands and pass-bands; see for example the pass-bands on the two sides of the $[\omega_{3.5^l}, \omega_{3.5^r}]$ stop-band. As a result, full-cycle stop-bands dominate the frequency response of the 5LD unit cell.

Next, the energy parameters of the 5LD unit cell are shown in Figs. 23 and 24. As expected, for the lossless unit cell a is identically zero in Fig. 23(a). A more interesting observation for this particular unit cell is that $r = 1$ ($t = 0$) for almost the entire widths of the full-cycle stop-bands; it is only close to pass-bands and half-cycle stop-bands that the unit cell is not a perfect reflector for the 5LD unit cell. The energy parameters for the η- and δ-models are shown in Fig. 23(a) and (c), respectively. For both models, high energy absorptions are observed in the half-cycle stop-bands and surrounding pass-bands. This aspect can more clearly be observed in Fig. 23(d), where a is plotted against the phase angle ϕ. Since a varies across the stop-bands, it does not take a unique value for $\phi = \pi(1 + 2p)$ and $\phi = 2\pi p$. However, it is clearly shown that highest values for a are achieved in half-cycle stop-bands ($\phi/\pi = 0.5 + p$) and pass-bands around them, and that a stays around zero in full-cycle stop-bands. It should be emphasized that high a values around half cycle stop bands is not true in general. For example, this is not the case for the 5LA unit cell (not shown here for brevity).

The energy loss characteristics of the two model can more clearly be compared in Fig. 23(d). The low, intermediate, and high loss parameters of the two models are chosen such that at high fre-

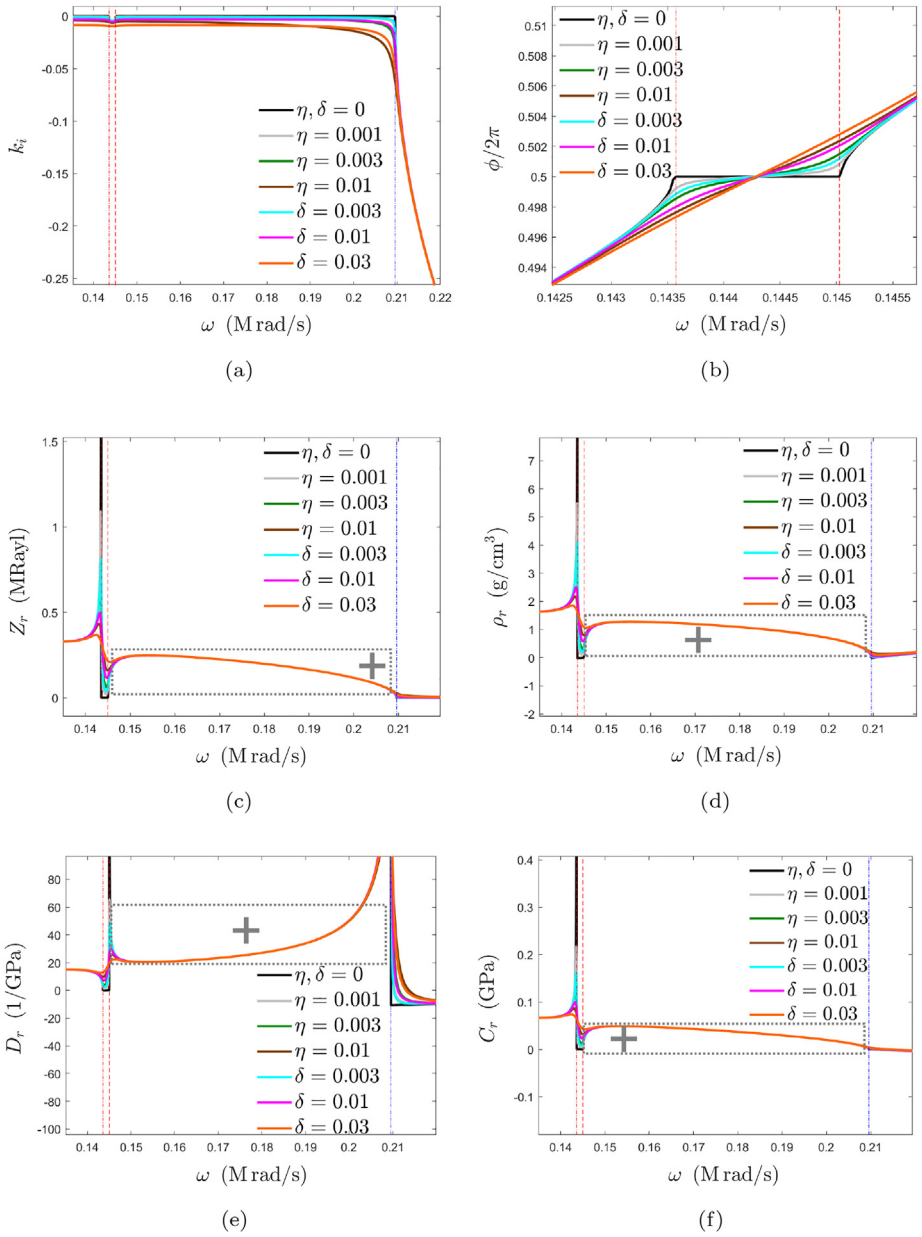

Fig. 20. The use of the solutions of unit cells with loss to determine the stable solution branch for retrieved material properties of the lossless 5LD unit cell.

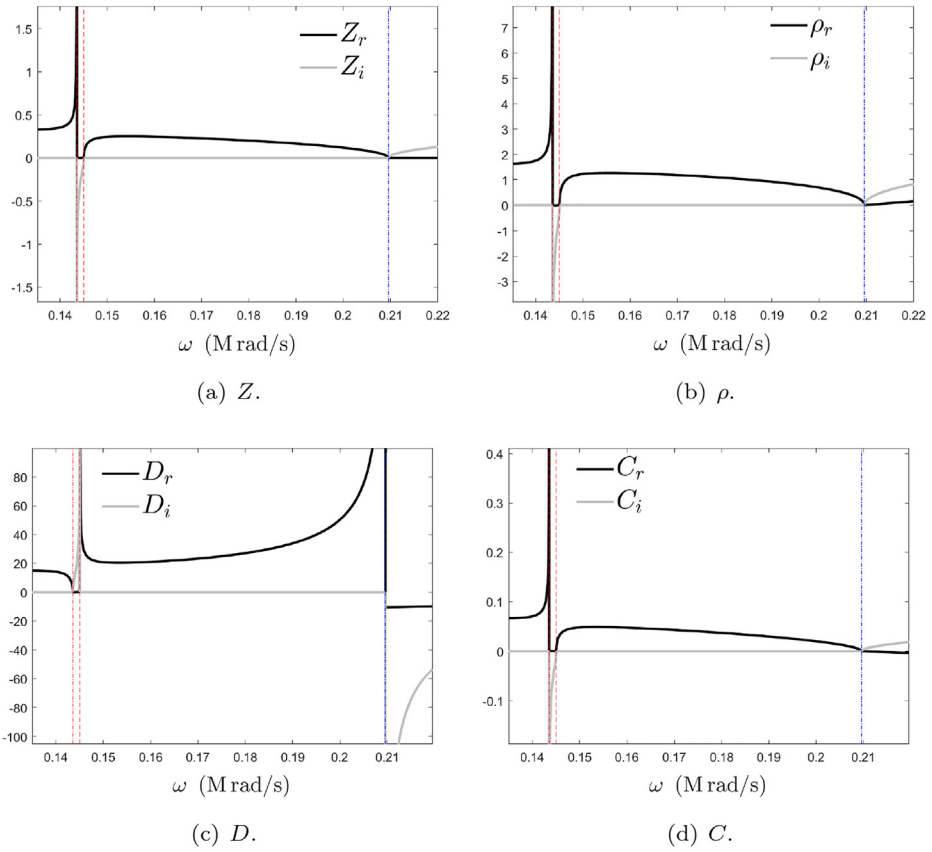

Fig. 21. Retrieved constitutive parameters for the lossless 5LD unit cell.

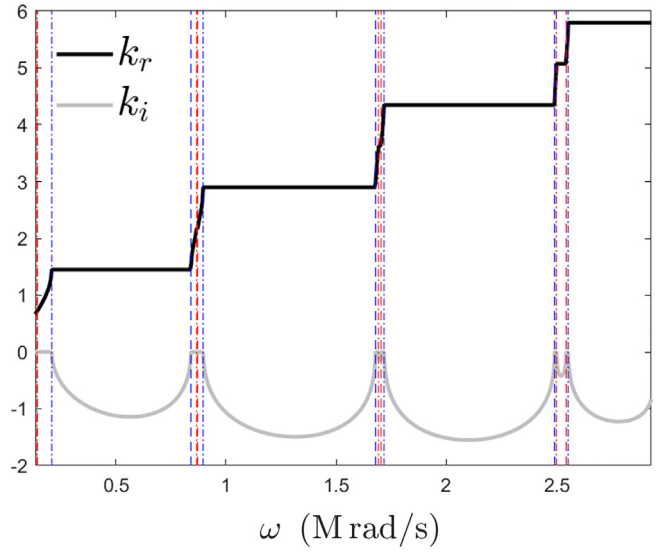

Fig. 22. Wavenumber for the lossless 5LD unit cell for $\omega \in [\omega_{0.5^l}, \omega_{4^l}] = [0.143575, 2.947275]$.

quencies they result in very similar loss parameters and retrieved constitutive parameters. This can be seen in the fourth half-cycle stop-band and surrounding pass-bands in Fig. 23(d) ($3 < \phi/2\pi < 4$), where the pairs of low, intermediate, and high loss parameters results in almost the same a. However, as we shift to lower frequencies, the δ-model becomes more lossy by exhibiting higher a values for each of the three pairs; see for example the zones $2 < \phi/2\pi < 3$ and $1 < \phi/2\pi < 2$ in the figure.

5. 2D photonic crystal example

5.1. Problem description for the 2D unit cell

In this section we consider a 2D photonic crystal studied in Nemat-Nasser (2019). The unit cell is a 10 mm $\times$ 10 mm aluminum square, containing a circular inclusion of PMMA with diameter 4.46 mm. The properties of the Aluminum matrix are Young's modulus $E_M = 68$ GPa, mass density $\rho_M = 2.7$ g/cm^3, and Poisson ration $\nu_M = 0.33$. The properties of polymethyl methacrylate (PMMA) inclusion are $E_I = 3$ GPa, $\rho_I = 1.2$ g/cm^3, and $\nu_I = 0.4$. The plane strain condition is assumed for this problem. We characterize this unit cell from zero to frequency $f = 300$kHz (corresponding to $\omega = 1.88$ M rad / s). The aSDG method and COMSOL are used for the TD and FD analysis of this unit cell; *cf.* Section 2.3.

The problem description and initial spatial discretization used for the TD analysis of this unit cell are shown in Fig. 25. The spatial triangulation is comprised of 1321 nodes and 2519 triangles. The domain is extended by 12 mm and 8 mm on the reflection and transmission sides, respectively, to represent the infinite ambient zones in the parameter retrieval method. Silver-Müller transmitting boundary condition is used in the ambient zones to terminate the computational domain. Material properties of the ambient zone are chosen identical to those of the matrix to reduce the simulation time $\overline{T}$, *cf.* Section 2.3, needed for the TD method. Symmetry boundary condition is used on the top and bottom boundaries of the domain. Since scatter field (SF) formulation is used in reflection side, and total field (TF) formulation is used in the unit cell and

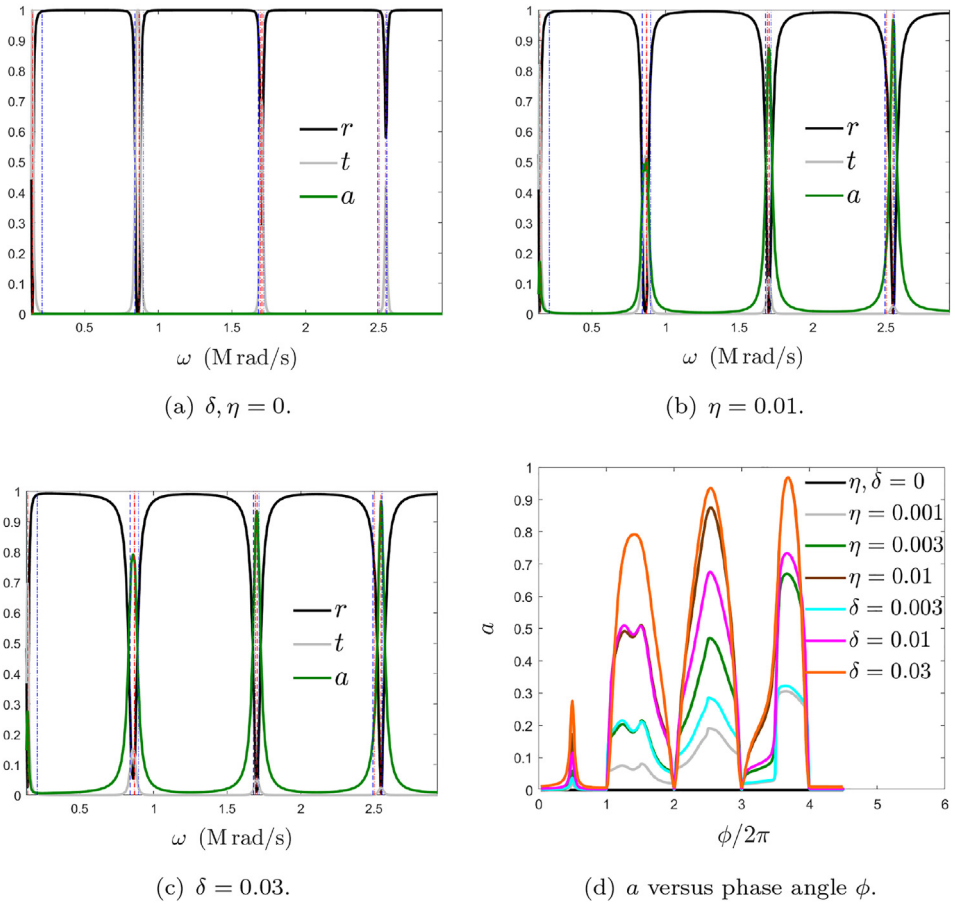

Fig. 23. The effect of the loss model on energy parameters of the 5LD unit cell for the frequency range $\omega \in [\omega_{0.5'}, \omega_{4'}] = [0.143575, 2.947275]$.

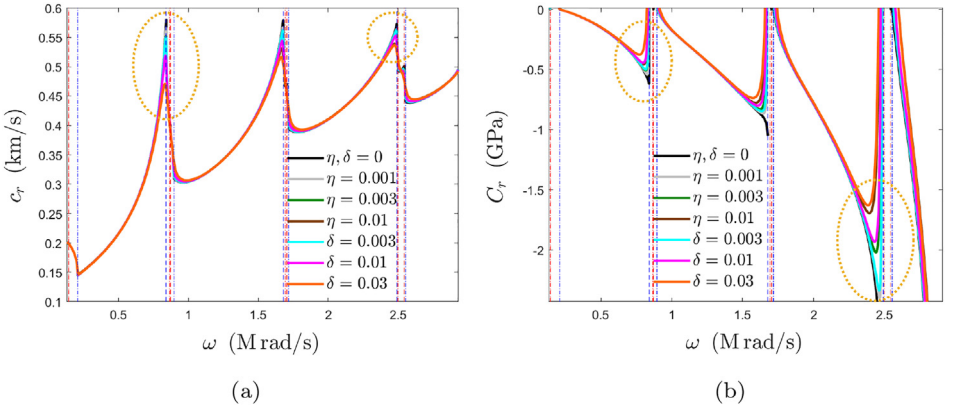

Fig. 24. The effect of loss model on sample retrieved parameters for the 5LD unit cell.

transmission side, special matching conditions are used on the blue interface between the two zones in the figure (Busch et al., 2011); *cf.* Section 2.3.

The parameters for the TD incident wave $\mathbb{I}(t)$ are $\omega_{\min} = -0.5$ M rad / s and $\omega_{\max} = 2.5$ M rad / s. This corresponds to $\omega_0 = 1$ M rad / s and $\varsigma = 2/3$ μs. The parameter n_0 is chosen as $n_0 = 4\varsigma = 8/3$ μs. The final time of the TD simulation if $\overline{T} = 184.56$ μs. As described in Section 2.3, the aSDG method gradually fills the 3D spacetime domain by each time solving a patch of tetrahedral elements. At the final time, the computational domain contains about 36 million elements arranged in more than 6.3 million patches.

5.2. Solution of the lossless 2D unit cell

The lossless unit cell is solved by the FD method with 3531 discrete frequencies in the frequency range of interest, with finer frequency steps around a narrow stop-band that will be discussed later. About 3760 discrete frequencies are used in the inverse Fourier transform of TD results. As in the preceding sections, the stable solution branches for the lossless unit cell are determined by using the solutions of lossy unit cells. The form of added loss is further discussed in Section 5.5. Due to the higher accuracy and adaptive resolution of frequency steps of the FD approach, only the FD solutions are presented here and in Section 5.4.

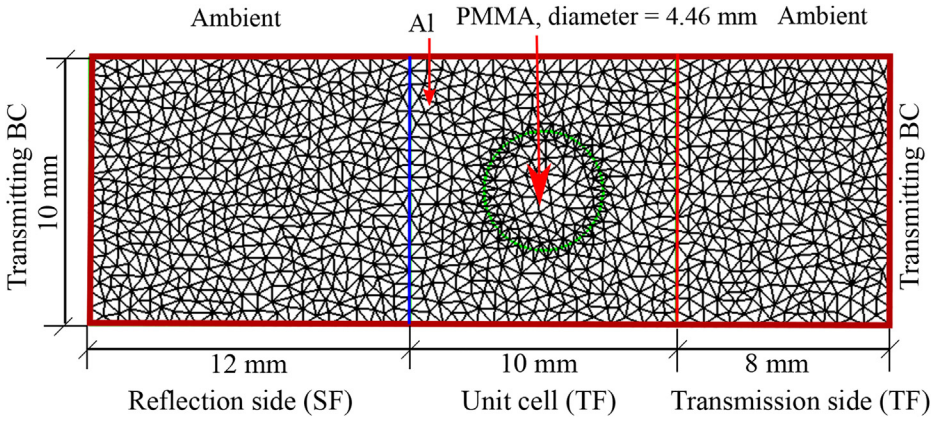

Fig. 25. Problem description and spatial mesh for the 2D unit cell and ambient zones on reflection and transmission sides for the aSDG method.

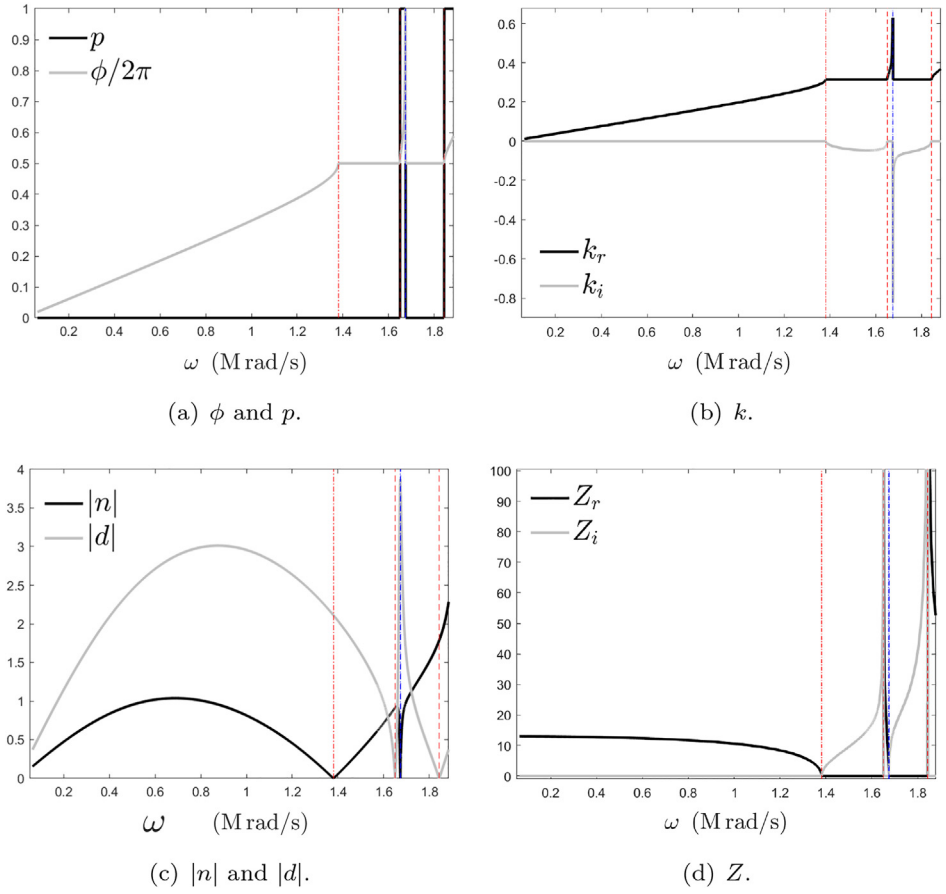

Fig. 26. The parameters ϕ and (n, d) needed to determine k and Z from (9) and (8) a, respectively, for the lossless 2D unit cell.

Table 3
End points of the stop-bands for the 2D unit cell.

Description	Symbol	Line marker	Value (M rad / s)
Start of the first half-cycle stop-band	$\omega_{0.5^l}$	– · – ·	1.38104
End of the first half-cycle stop-band	$\omega_{0.5^r}$	– – – –	1.65059
Start of the first full-cycle stop-band	ω_{1^l}	– · – ·	1.67346
End of the first full-cycle stop-band	ω_{1^r}	– – – –	1.67516
Start of the second half-cycle stop-band	$\omega'_{0.5^l}$	– · – ·	
End of the second half-cycle stop-band	$\omega'_{0.5^r}$	– – – –	1.84349

Fig. 26 shows the retrieved k and Z for the lossless 2D unit cell. As shown in Fig. 26(a), ϕ increases to π at $\omega_{0.5^l} = 1.38104$, the beginning of the first half-cycle stop-band. This is followed by a narrow pass-band from the end of this stop-band at $\omega_{0.5^r} = 1.65059$ to the beginning of a very narrow full-cycle stop-band at $\omega_{1^l} = 1.67346$. Interestingly, for this unit cell, ϕ sharply drops from 2π to π at the end of this stop-band at $\omega_{1^r} = 1.67516$. Thus, there is a secondary half-cycle stop-band with again $\phi = \pi$ from $\omega'_{0.5^l} = \omega_{1^r}$ to $\omega'_{0.5^r} = 1.84349$. These frequencies and their corresponding line markers are shown in Table 3. Since the narrow full-cycle stop-band in $[\omega_{1^l}, \omega_{1^r}]$ cannot be clearly seen in these figures, the solution in this stop-band and the nature of sudden decrease of ϕ is further discussed in Section 5.4.

Fig. 26(c) shows the relation between zero points of n and d and the end points of the stop-bands. For all 1D unit cells presented in Section 4, half-cycle stop-bands start when $d = 0$ and end when $n = 0$. For full-cycle stop-bands this reverses in that the start and end frequencies correspond to $n = 0$ and $d = 0$, respectively. Clearly, the same trends are not observed for the 2D unit cell in Fig. 26(c). For example, for the first half-cycle stop-band, $n = 0$ at $\omega_{0.5^l}$ and $d = 0$ at $\omega_{0.5^r}$; this results in a similar variation of retrieved parameters to those of the full-cycle stop-bands of 1D unit cells in Section 4. It appears that having a lighter and more compliant core for this example contributes to these features, providing the intriguing possibility of designing 1D systems with a similar response; for some examples of designing 1D systems with special properties, please refer to Mokhtari et al. (2019). Furthermore, while not clear in the figure, the first full-cycle stop-band also starts with condition $n = 0$ at ω_{1^l}. As will be discussed in Section 5.4, neither n nor d are zero at the end of this stop-band, which coincides start of the next half-cycle stop-band at $\omega_{1^r} = \omega'_{0.5^l}$. Finally, the second half-cycle stop-band ends with condition $d = 0$ at $\omega'_{0.5^r}$, *i.e.,* similar to the end condition of full-cycle stop-bands in Section 4.

Fig. 26(d) shows the retrieved impedance for the lossless 2D unit cell. While not shown, similar to Fig. 8(b), n/d is real positive in pass-bands and real negative in stop-bands. This results in zero Z_r and Z_i in stop-bands and pass-bands, respectively; *cf.* (8) a. At

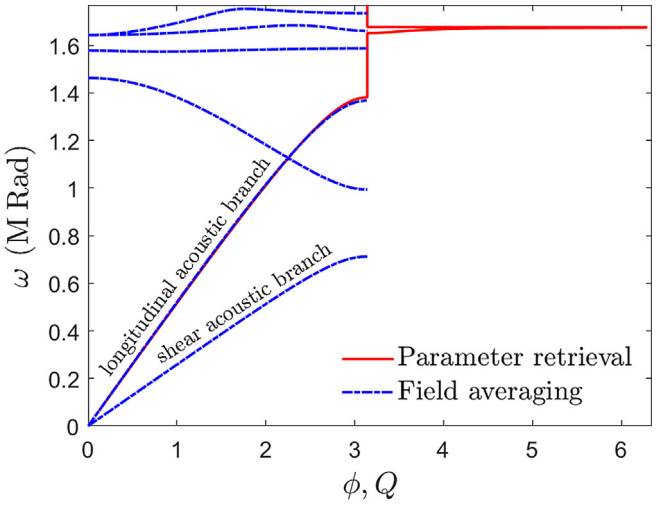

Fig. 28. Comparison of band structures constructed by the scattering and Bloch eigenvalue analyses.

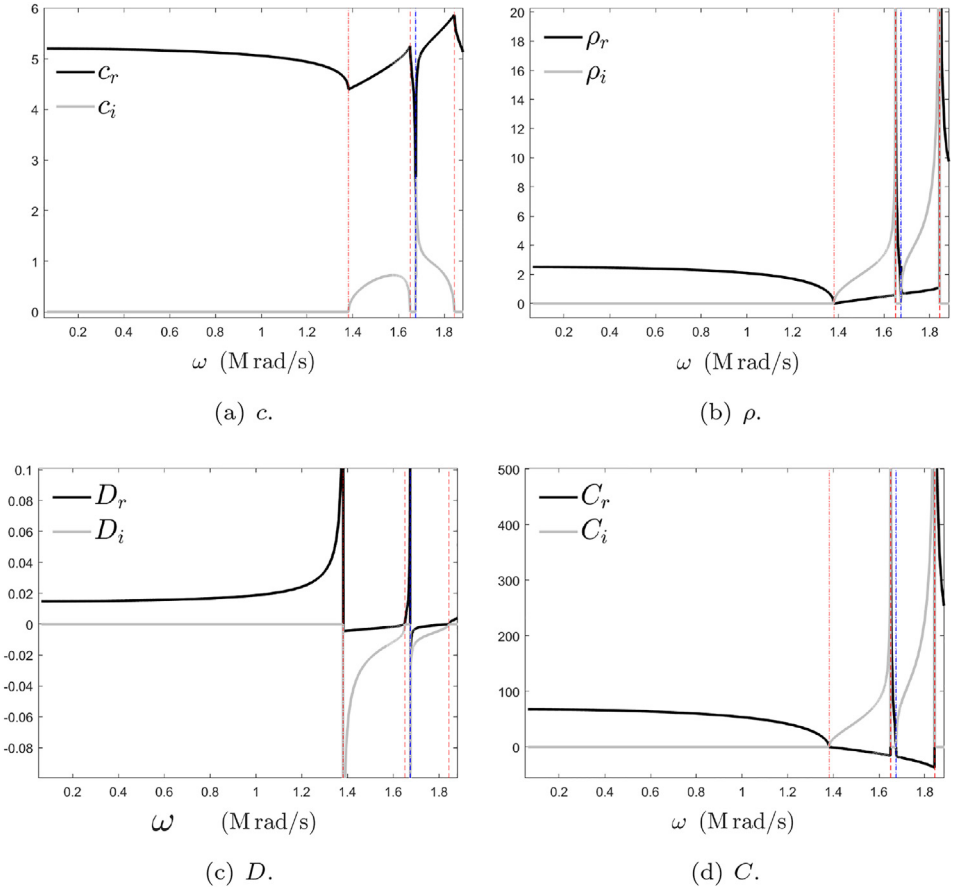

Fig. 27. Retrieved constitutive parameters for the lossless 2D unit cell.

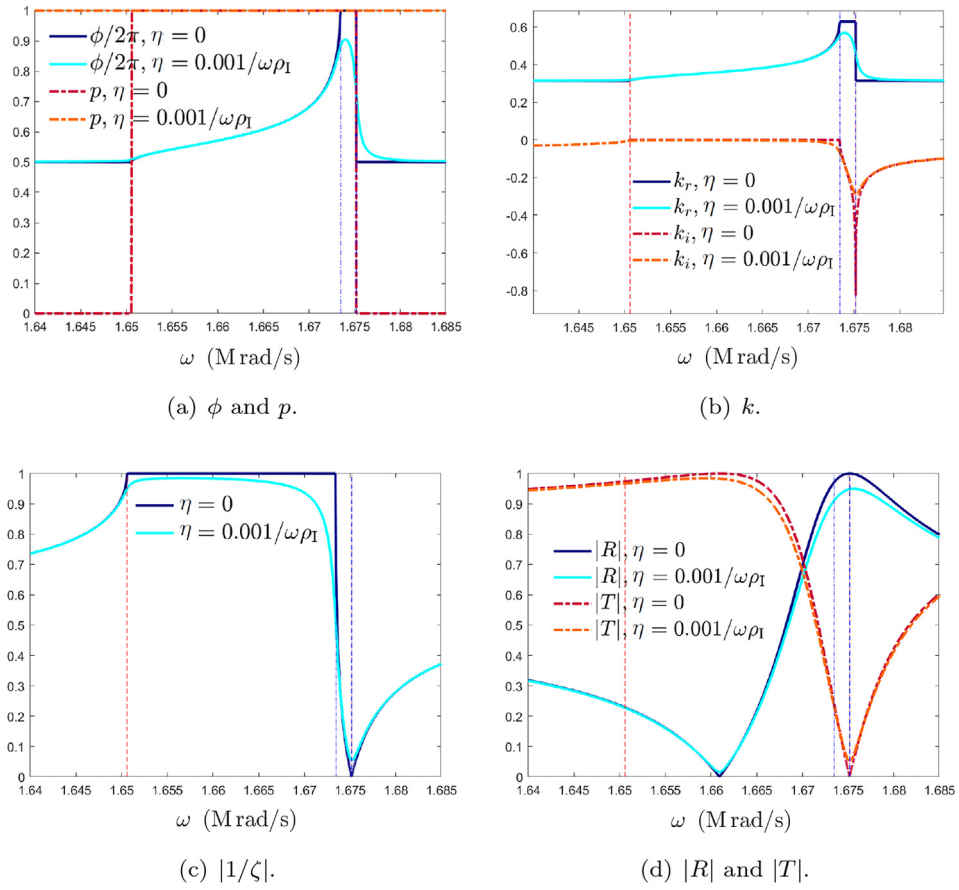

Fig. 29. The appearance of the very narrow first full-cycle stop-band in $[\omega_{1^l}, \omega_{1^r}]$ and parameters contributing to the value of k for the 2D unit cell.

the boundaries of stop-bands for which $n = 0, Z$ is zero. Finally, Z_r and Z_i take infinite limits outside the stop-bound boundaries for which $d = 0$.

The retrieved constitutive parameters for the lossless 2D unit cell are shown in Fig. 27. The real part of retrieved parameters are finite and single negative in stop-bands (ρ versus D/C). Moreover, the zero and infinite limits of Z in Fig. 26(d) dictate infinite limits of retrieved parameters; that is, infinite limits for ρ_r and C_r in pass-bands right after $\omega_{0.5^r}$ and $\omega'_{0.5^r}$, where $d \to 0$ and infinite limit for D_r in pass-bands before $\omega_{0.5^l}$ and ω_{1^l} where $n \to 0$. Finally, ρ and C tend to their quasi-static limits of 2.47 g/cm^3 and 67.7 GPa, respectively, as $\omega \to 0$.

5.3. Comparison of scattering and Bloch eigenvalue analyses

In Section 1, the field averaging and parameter retrieval methods were presented as two methods that can characterize overall dispersive properties of micro-structured media. The former is generally based on the Bloch wave representation and the latter relies on the scattering parameters of one or a number of unit cells sandwiched by an ambient medium. The purpose of this section is to compare the scattering approach used in this paper with the Bloch wave solution for the considered 2D unit cell.

Fig. 28 compares the band structure obtained by the scattering and Bloch eigenvalue analyses, where ω is plotted against $\phi = k_r l$ or the normalized wavenumber $Q := \mathrm{mod}(\phi, \pi)$. For the Bloch analysis, as described in Aghighi et al. (2019), the band structure is formed by solving discrete eigenvalues ω for any given k in the horizontal direction in Fig. 25. As shown in Fig. 28, there is a very good agreement between the solutions along the longitudinal acoustic branch and small deviations can only be observed right before the start of the first stopband at $\omega_{0.5^l}$. Since in the scattering approach, we have only considered the retrieval of material parameters pertained to longitudinal wave propagation, it cannot reproduce the shear mode solutions of the Bloch eigenvalue analysis in the figure.

The eigenvalue band structure provides interesting insights that may be quite complementary to scattering calculations. It must be noted that while we deal with a discrete branch ambiguity in k, it is still determined as a function of frequency in Fig. 26(b). In the scattering phase data, there is a discontinuous drop after a sharp but continuous rise in ϕ. Around the same frequency, the eigenfrequency calculations show a very feature-rich structure.

A few remarks are provided to conclude the comparison of scattering and Bloch wave eigenvalue analysis methods. First, as shown in Amirkhizi (2017) for 1D laminated systems there is a perfect match between the two approaches when normal incident waves are considered. More recently, Amirkhizi and Alizadeh (2018) shows a similar matching between the two methods for 1D laminated systems for oblique incidence of anti-plane shear waves.[2] This has been the rationale to compare the two methods only for this 2D example, where the results can differ. Second, while the matching is not perfect for 2D unit cells, our preliminary results (not presented here) show that once the number of unit cells is beyond a certain small limit (*e.g.*, 5), the results of scattering of finite

[2] For oblique incident waves, while the solution of the two approaches match, as shown in Amirkhizi and Alizadeh (2018) the overall constitutive law need be spatially dispersive. For 2D periodic media oblique waves also lead to diffraction and interface waves (Willis, 2016; Mokhtari et al., 2020). Since only normal incident waves are considered herein, these aspects are not further elaborated in this paper.

thickness slabs, become very close to the eigen-analysis predictions of an infinite domain, with most deviation occurring near resonances. For very small number of unit cells, this difference is observed even in long wavelength limit. Still, for this particular example, as shown in Fig. 28, there is a good match between the two methods for longitudinal modes even when one unit cell is used in the scattering method.

5.4. A narrow full-cycle stop-band

The solution details in the short frequency range of $[\omega_{0.5^r}, \omega_{1^r}]$ is discussed in this section. To choose the *stable* solution branch for the lossless unit cell, we introduce loss in the PMMA inclusion phase. For the FD approach, we employ a frequency-dependent model for η that resembles a constitutive model with nonzero damping coefficient for PMMA. If in (15), the terms $\delta\dot{u}$ and $Cu_{,xx}$ are lumped to a complex modulus, the ratio $\eta = C_i/C_r$ is $\omega\delta/k^2C$. By first order approximation of c by $\sqrt{C/\rho}$, the wave speed of lossless material, a damping-based η is approximated as $\eta = \delta/\rho\omega$. The rather constant and linear dependence of a on δ and η in Section 3 also imply that $\eta \propto 1/\omega$ would resemble a damping model. A value of $\delta = 0.001$ g/cm^3 μs is used for the lossy unit cell herein.

Fig. 29 is used to show the existence of a very narrow full-cycle stop-band and the discontinuity of ϕ at its end point. Fig. 29(a)

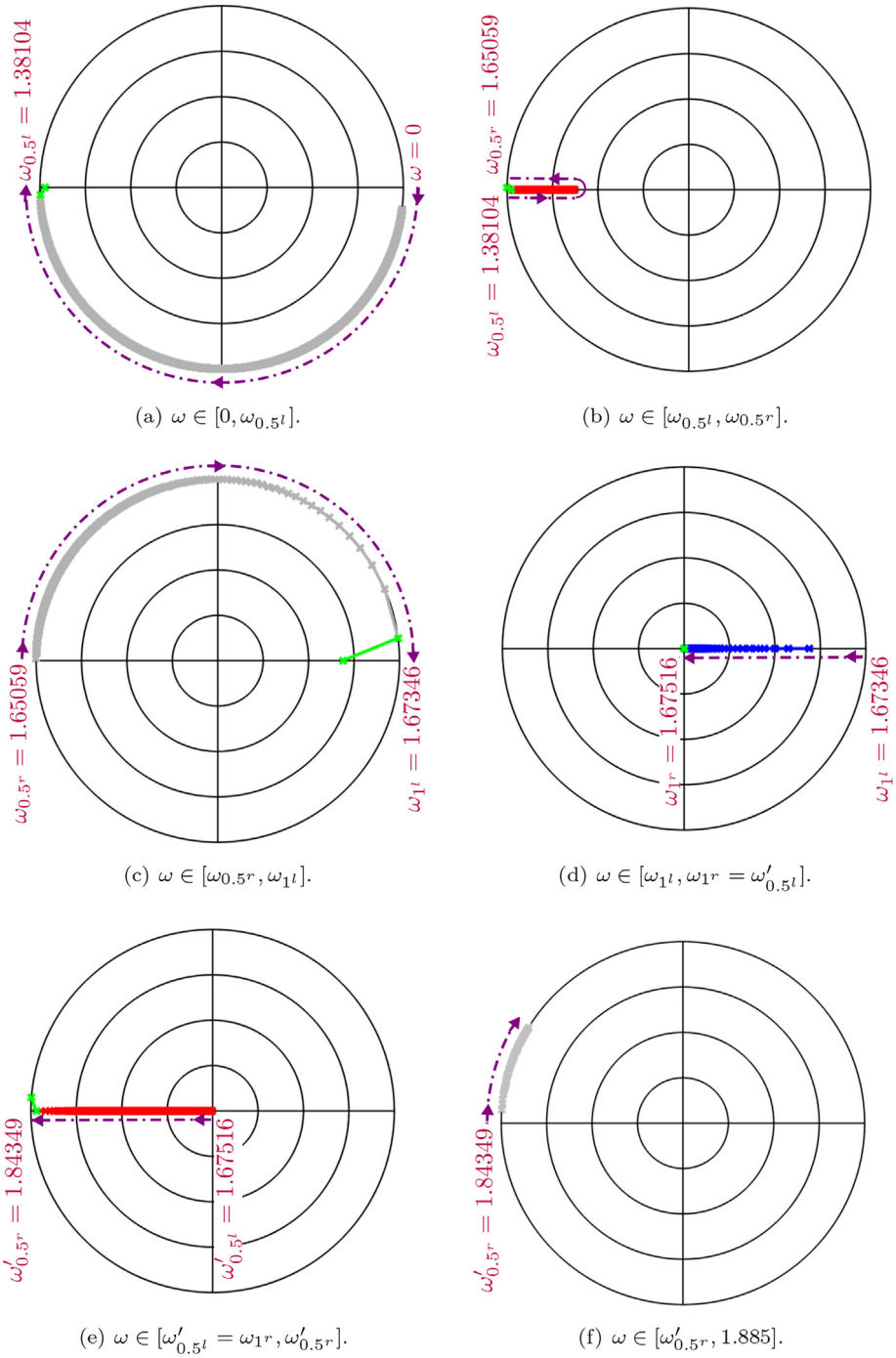

(a) $\omega \in [0, \omega_{0.5^l}]$. (b) $\omega \in [\omega_{0.5^l}, \omega_{0.5^r}]$.

(c) $\omega \in [\omega_{0.5^r}, \omega_{1^l}]$. (d) $\omega \in [\omega_{1^l}, \omega_{1^r} = \omega'_{0.5^l}]$.

(e) $\omega \in [\omega'_{0.5^l} = \omega_{1^r}, \omega'_{0.5^r}]$. (f) $\omega \in [\omega'_{0.5^r}, 1.885]$.

Fig. 30. The phase space of $1/\zeta$ at the end of pass-bands and stop-bands for $\phi = \pi_-, \pi_+, 2\pi_-, 2\pi_+$ for 2D unit cell. The red and blue segments on negative and positive real axes, correspond to half- and full-cycle stop-bands, respectively. Arrows on the purple dotted-dashed line show the direction at which ω increases.

shows how the lossy solution is used to determine p for the stable solution, hence ϕ, for the lossless unit cell. In the pass-band $[\omega_{0.5^r}, \omega_{1^l}]$ of 3.64 kHz range, phase angle quickly increases from π to 2π. This is followed by the narrow stop-band $[\omega_{1^l}, \omega_{1^r}]$ of width 28 Hz, for which $\phi = 2\pi$. Similar to the examples in Section 4, the lossy solution is used to choose an increasing, rather than decreasing, ϕ solution in the pass-band $[\omega_{0.5^r}, \omega_{1^l}]$. Moreover, a unique feature of this unit cell is the abrupt change of ϕ at ω_{1^r}. In contrast, ϕ remains continuous for the lossy unit cell, though if loss is reduced, the behavior will approach more and more to the sharp discontinuous decrease in the lossless system. The decrease of ϕ for the lossy unit cell determines that ϕ should also decrease for the lossless unit cell at ω_{1^r}. This rules out a nonphysical solution for lossless unit cell for which ϕ jumps up to 3π at ω_{1^r}. Note that in previous examples in this paper, ϕ was always a monotonously increasing function of ω. The corresponding k_r values are shown in Fig. 29(b).

Next, we discuss the special properties of retrieved properties at ω_{1^r}, where k is discontinuous. As expected, $|1/\zeta|$ takes a unit value in the pass-band $[\omega_{0.5^r}, \omega_{1^l}]$, resulting in $k_i = 0$; *cf.* 9. A more interesting observation is the decrease of $|1/\zeta|$ from one to zero in the stop-band. For the discrete set of frequencies the unit cell is analyzed, the value of $|1/\zeta|$ gets as small as 2.6×10^{-4}. As will be discussed next, Z is imaginary and nonzero at ω_{1^r}; *cf.* Fig. 32(b). Thus, from (8) b, T must tend to zero at ω_{1^r} to accommodate a zero limit for $|1/\zeta|$ at this point. This is verified in the plot of T in Fig. 29(d).

To better demonstrate the nature of this jump, the evolution of $1/\zeta$ up to $\omega = \omega'_{0.5^r}$ is shown in complex plane in Fig. 30. At the beginning of the first stop-band, $1/\zeta = -1$ at $\omega = \omega_{0.5^l}$ in Fig. 30 (a). Through this stop-band negative real $1/\zeta$ gets closer to zero and recovers a unit value at the end of the first stop-band at $\omega = \omega_{0.5^r}$ in Fig. 30(b). This corresponds to the dip in k_i for $\omega \in [\omega_{0.5^l}, \omega_{0.5^r}]$ in Fig. 26(b). Past this frequency, both $1/\zeta$ and k smoothly vary until the start of the full-cycle stop-band at Fig. 30 (c). This is similar to the continuous change of both parameters for 1D unit cells in Section 4; *cf.* for example Fig. 11. The evolution of $1/\zeta$, however, is different for the first full-cycle stop-band. Through this stop-band positive real $1/\zeta$ tends from one to zero as shown in Fig. 30(d) (as discussed in Section 4.2, the pass- and stop-band green connecting segments demonstrate the discrete nature of sampled frequencies). Unlike all previous examples of full-cycle stop-bands, $1/\zeta$ does not increase to one at the transition point to the next pass-band. Rather, $1/\zeta$ passes through zero to negative real axis at the transition to the second half-cycle stop-band at ω_{1^r}. ζ crossing the 0 value, is equivalent to $k_i \to -\infty$. The change of $1/\zeta$ from zero to -1 in the second half-cycle stop-band is shown in Fig. 30(e). Fig. 31 shows how by adding loss, $1/\zeta$ moves farther away from the origin and its maximum attained argument decreases. These result in lower values for $|k_i|$ and maximum value of k_r, respectively, for $\eta = 0.001/\rho_I\omega$ around $[\omega_{1^l}, \omega_{1^r}]$ in Fig. 29(b).

In short, we believe that for the lossless unit cell, at the transition point between the full- and half-cycle stop-bands, $T = 0$ and

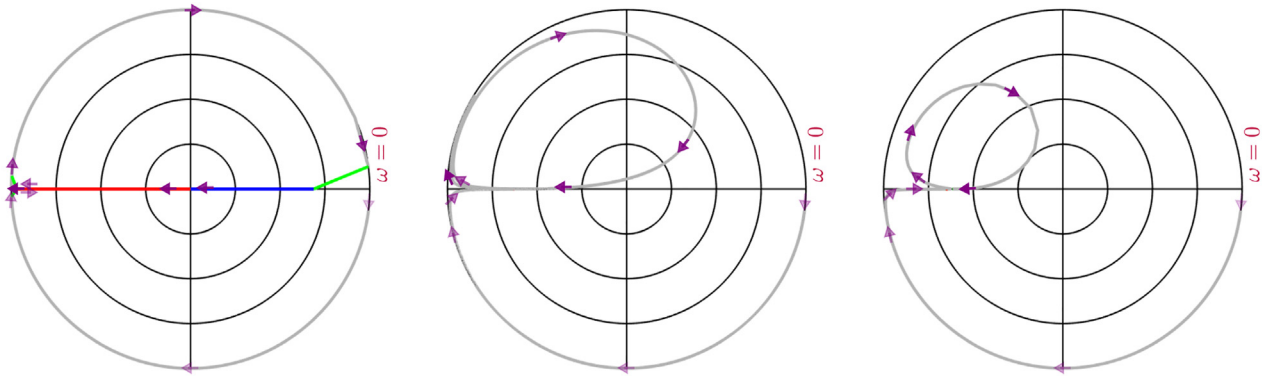

(a) Lossless unit cell at $\omega = \omega'_{0.5^r} = 1.84349$. (b) $\eta = 0.001/\rho_I\omega$ unit cell at $\omega = 1.885$. (c) $\eta = 0.01/\rho_I\omega$ unit cell at $\omega = 1.776$.

Fig. 31. The effect of loss on phase space of $1/\zeta$ for the 2D unit cell at comparable frequencies. Arrows, shaded from light to dark purple from $\omega = 0$ to higher values show the direction at which ω increases.

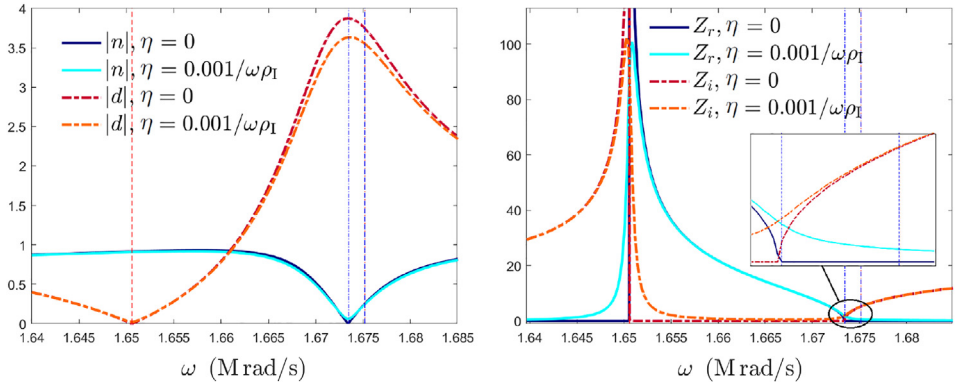

(a) $|n|$ and $|d|$. (b) Z.

Fig. 32. The parameters n and d needed to determine Z from (8) a, and Z around the first full-cycle stop-band for the 2D unit cell.

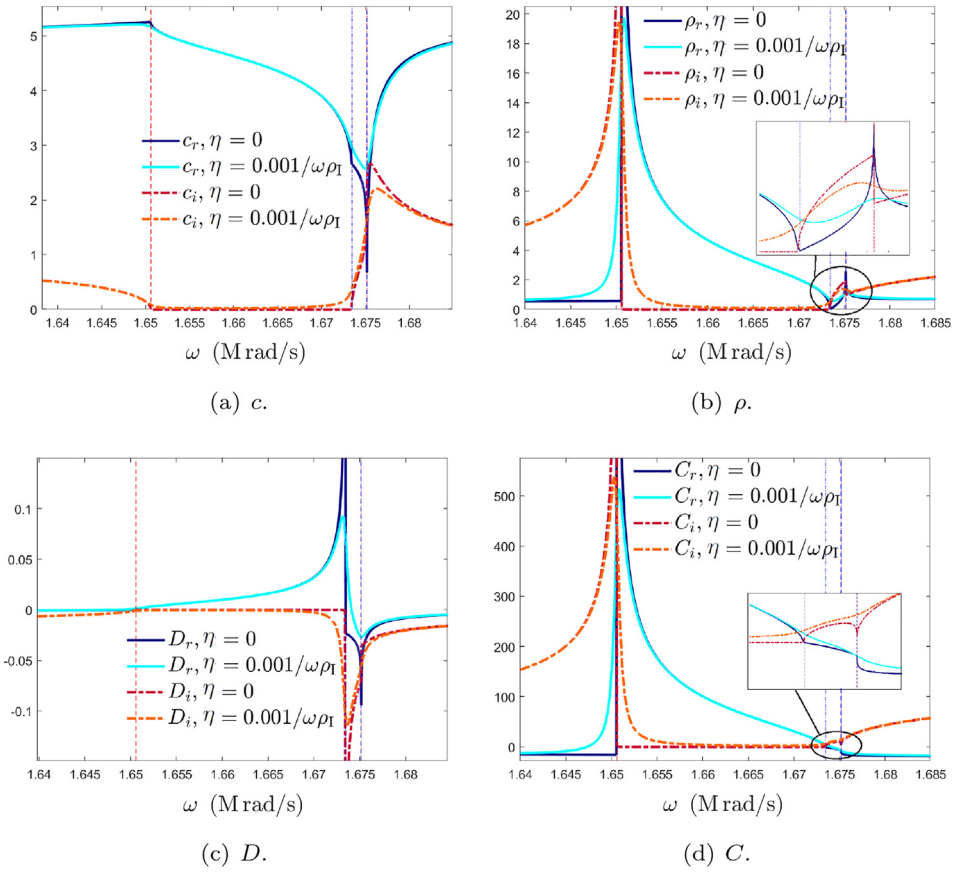

Fig. 33. Retrieved constitutive parameters for the 2D unit cell around the first full-cycle stop-band.

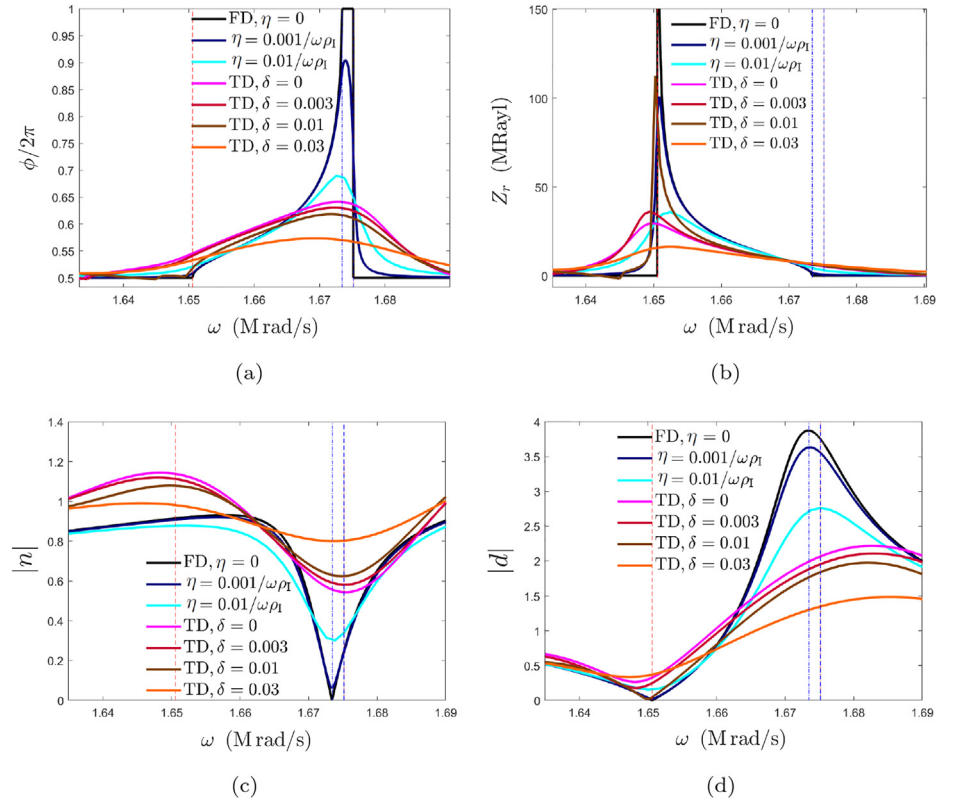

Fig. 34. Comparison of the effect of loss in retrieved ϕ and Z_r for the TD and FD methods.

$1/\zeta$ transitions from positive to negative real axis. This example demonstrate the inability of methods that are based on continuity of k, *e.g.*, (Arslanagić et al., 2013; Shi et al., 2016), in capturing the stable solution branch in general. However, all retrieved properties of lossy unit cells are continuous and their solution can be used to determine the stable solution branch for lossless unit cells, even when k is discontinuous (in this case the real part expressing a finite jump, while the imaginary part becomes unbounded).

The retrieved $|n|$ and $|d|$ around the first full-cycle stop-band are shown in Fig. 32(a). As mentioned before, the full-cycle stop-band starts with $n = 0$ at ω_{1^l}. However, at ω_{1^r} neither n nor d are zero. Accordingly, unlike the other end points of stop-bands Z is finite and nonzero at this point; as shown in Fig. 32(b), Z is imaginary and continuous in this and subsequent stop-bands. The other retrieved constitutive parameters for the lossless and lossy unit cell are shown in Fig. 33. Since Z is nonzero and finite at ω_{1^r}, ρ, D and ρ all are finite and nonzero at this frequency. However, the jump in k_r results in jumps in the slope and/or values of these quantities; *cf.* for example jumps in ρ_r and C_r at ω_{1^l} in Fig. 33(b, d).

5.5. Comparison of TD and FD solutions for lossy unit cells

The use of the damping-based model of $\eta = \delta/\rho_l\omega$ for the FD simulations enables objective comparison of the FD method with the aSDG TD method. For the TD approach, damping values of $\delta = 0.003, 0.01, 0.03$ g/cm^3 μs are used in the PMMA phase. For the FD method, beside the lossless solution, unit cells with $\delta = 0.001$ g/cm^3 μs and $\delta = 0.01$ g/cm^3 μs are used for the PMMA phase in $\eta = \delta/\rho_l\omega$.

Figs. 34 and 35 compare the two approaches in terms of the retrieved parameters. As shown in 34(a), the FD solutions for ϕ are closer to that of the lossless unit cell. Even the solution for the lossless TD solution is farther away than the lossy FD solutions from the lossless FD solution. The same trends are observed in Fig. 35, with the exception of more accurate solutions for $\delta = 0.01$ of the TD approach around $\omega_{0.5^r}$. This can be explained with unusually closer to zero $|d|$ value for this solution in 34(d). This results in closer values to those of the lossless unit cell for Z_r and as a result ρ_r and C_r for this solution around $\omega_{0.5^r}$. However, aside from this region, TD solutions are farther away from the solutions of lossless unit cell, even for comparable loss parameters (*e.g.*, $\delta = 0.01$). This implies that the numerical dissipation of TD solution dominates the effect of added loss on retrieved parameters in such low loss systems.

Finally, two of the energy parameters of the unit cell are shown in Fig. 36. As expected, $t = |T|^2$ moves away from zero around ω_{1^r}, where $T = 0$ was deemed to be the cause of discontinuity of k for the lossless unit cell. The absorbance solutions are compared in Fig. 36(b) for a wider frequency range. As in all previous examples, largest losses are encountered in regions with fastest changes in retrieved properties, that is around $[\omega_{0.5^r}, \omega_{1^l}]$. For the lossless and low damping TD solutions, a achieves large negative values (energy gain) near the full-cycle stop-band. While the aSDG method is energy dissipative (Abedi, 2010), the non-negative energy loss is only guaranteed for an entire TD solution; thus, numerical gains for individual frequency bands in Fig. 36(b) does not violate the properties of the aSDG method.

Large energy errors (local frequency bands of gain) and relative insensitivity of retrieved parameters to damping value for the TD solutions suggest that this approach is not extremely efficient for the parameter retrieval method when drastic changes occur over very narrow frequency bands. However, for high frequencies, the TD method demonstrates its computational value and efficiency. Herein, to accurately capture the solution, a frequency step of 1 Hz is used around the narrow stop-band $[\omega_{1^l}, \omega_{1^r}]$. We also note

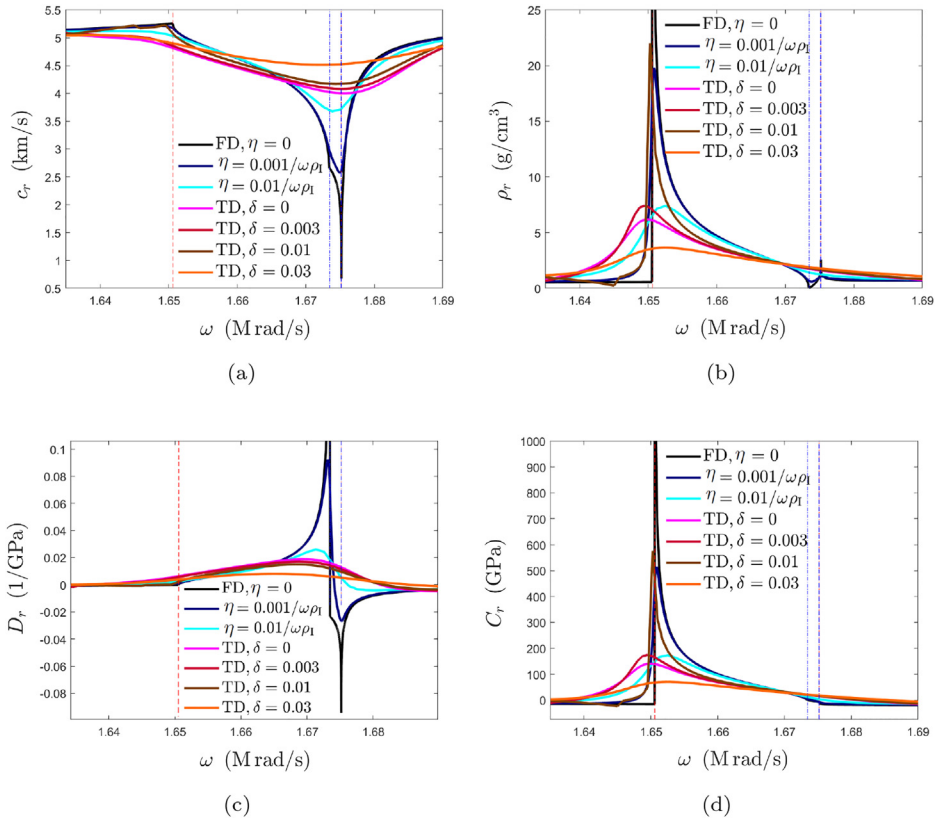

Fig. 35. The effect of added loss for the TD and FD methods in smoothening the response of retrieved parameters for the 2D unit cell.

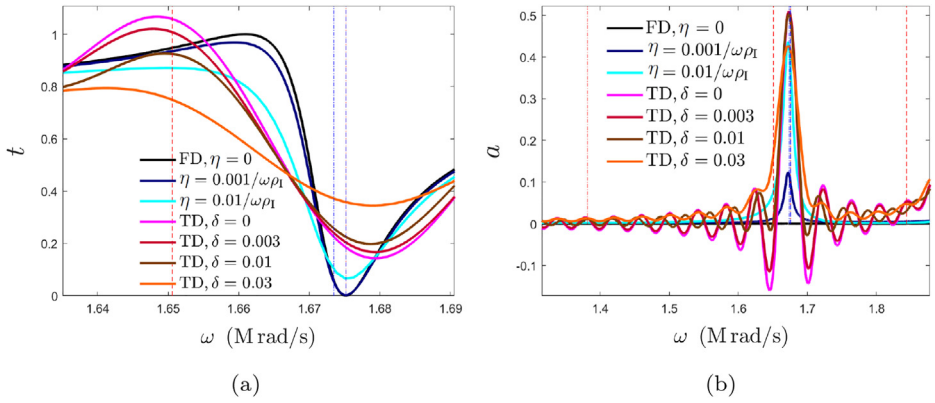

(a) (b)

Fig. 36. The effect of added loss for the TD and FD methods on energy parameters of the 2D unit cell.

that numerical difficulties were encountered when using the retrieval method described in Section 2.2, given the very low transmission values. Instead, the more robust parameter retrieval method of Amirkhizi (2017), suitable for Willis-type constitutive equations, was used in this frequency range.

6. Conclusions

We proposed the use of added loss as a means to determine *stable* solution branches of dispersive properties of lossless unit cells. The η- and δ-models are more appropriate for FD and TD methods, respectively, where loss is introduced through using complex modulus and nonzero damping values. We draw distinction between constant η being bad and frequency-dependent η being able to capture the physics somewhat more adequately. The two models were first compared for a 1D homogeneous medium. The two loss models are then compared for a finite length of material. In terms of energy characteristics the δ-model is more appropriate in that beyond very small frequencies the absorbance is rather constant, whereas for the η-model, absorption increases linearly versus frequency. When retrieved constitutive parameters are concerned, however, the η-model results in a uniform error across frequencies, whereas for the δ-model large errors are encountered as frequency tends to zero. The two models were also compared for more complex 1D and 2D unit cells.. Consistent with earlier analyses, δ-model resulted in larger losses and errors in retrieved properties (relative to those of a lossless unit cell) as frequency tended to zero.

For the lossless unit cells, the half- and full-cycle stop-bands refer to regions for which $\phi = \pi + 2p\pi$ and $2\pi + 2p\pi$, respectively. For the 1D unit cells considered, impedance was infinite in the beginning of half-cycle and end of full-cycle stop-bands and zero at their other end points. This resulted in infinite limits for ρ_r and C_r before half-cycle and after full-cycle stop-bands and infinite limits for D_r after half-cycle and before full-cycle stop-bands. As discussed in Section 5.2, other designs of 1D systems may alter the aforementioned structure of stop-bands; an aspect that is not further investigated herein. As expected, retrieved materials were single negative in stop-bands with finite values for their real components. For a 5-layer unit cell, it was shown that both double-positive and double-negative (DN) solutions were valid pointwise in a pass-band. However, we used the lossy solutions to show that only the double negative solution was stable. This was based on achieving unstable (in the sense defined in Section 2.2) positive value of k_i for the DN solution. In addition, even for the lossy solutions k, Z, and various retrieved constitutive parameters had to suffer jump if the solution branch corresponding to the DN lossless unit cell were to be used. As shown, both loss models were effective to determine the stable solution branches.

Several aspects of the 2D unit cell were different from the analyzed 1D unit cells. First, there was no consistency in terms of infinite and zero limits of impedance at the end frequencies of half- and full-cycle stop-bands. Second, the phase angle and consequently wavenumber both suffered jumps at the end of a very narrow full-cycle stop-band. Third, ϕ was not a non-decreasing function of frequency given that a secondary stop-band with $\phi = \pi$ was observed right after this full-cycle stop-band with $\phi = 2\pi$. Some of the special properties at the end of this stop-band are having a finite and nonzero impedance value, as well as a limiting zero transmission coefficient, and transition of $1/\zeta = e^{-kl}$ from real positive to real negative axis. While existing proposed methods to choose the stable solution branch by preserving the continuity of k fail for this problem, we demonstrated that taking the limit of the solution of lossy-unit cells, when loss tends to zero, can successfully capture all such solution features.

Declaration of Competing Interest

The authors declare that they have no known competing financial interests or personal relationships that could have appeared to influence the work reported in this paper.

Acknowledgements

Abedi acknowledges partial support for this work via the U.S. National Science Foundation (NSF) CCF – Scalable Parallelism in the Extreme (SPX) program Grant No. 1725555 to the University of Tennessee Space Institute. Amirkhizi acknowledges support from the U.S. NSF, Civil, Mechanical and Manufacturing Innovation (CMMI) program Grant No. 1825969 to the University of Massachusetts, Lowell.

Appendix A. Other arguments for choosing the stable branch for 5LD

In Section 4.3, taking the limit of the solution of lossy unit cells was used to determine the stable branch in the frequency range $I_w := [\omega_{0.5^r}, \omega_{1^t}] = [0.145025,\ 0.209575]$ for the 5LD unit cell; *cf.* Fig. 20. In this appendix, it is shown that the continuity of retrieved parameters for lossy unit cells can also be used to determine the stable branch in I_w.

First, solutions for k_i are shown in Fig. 37 for the three branches (solutions for $+, p = 0$ and $+, p = 1$ match) and zero and nonzero loss parameters (damping in P_2). The continuity of k can be used

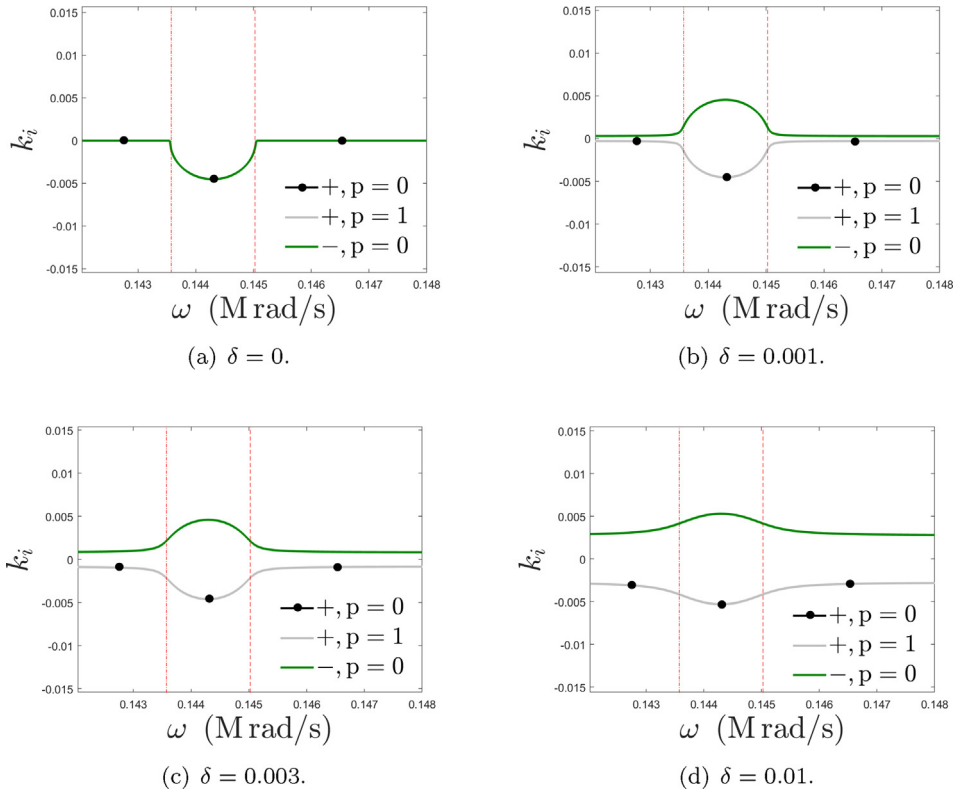

(a) $\delta = 0$. (b) $\delta = 0.001$.

(c) $\delta = 0.003$. (d) $\delta = 0.01$.

Fig. 37. Demonstration that for a 5LD unit cell with loss, the negative branch is invalid in I_w given that the corresponding $k_i > 0$ and transition between + and − branches $(p = 0)$ results in a jump in k_i for lossy unit cells.

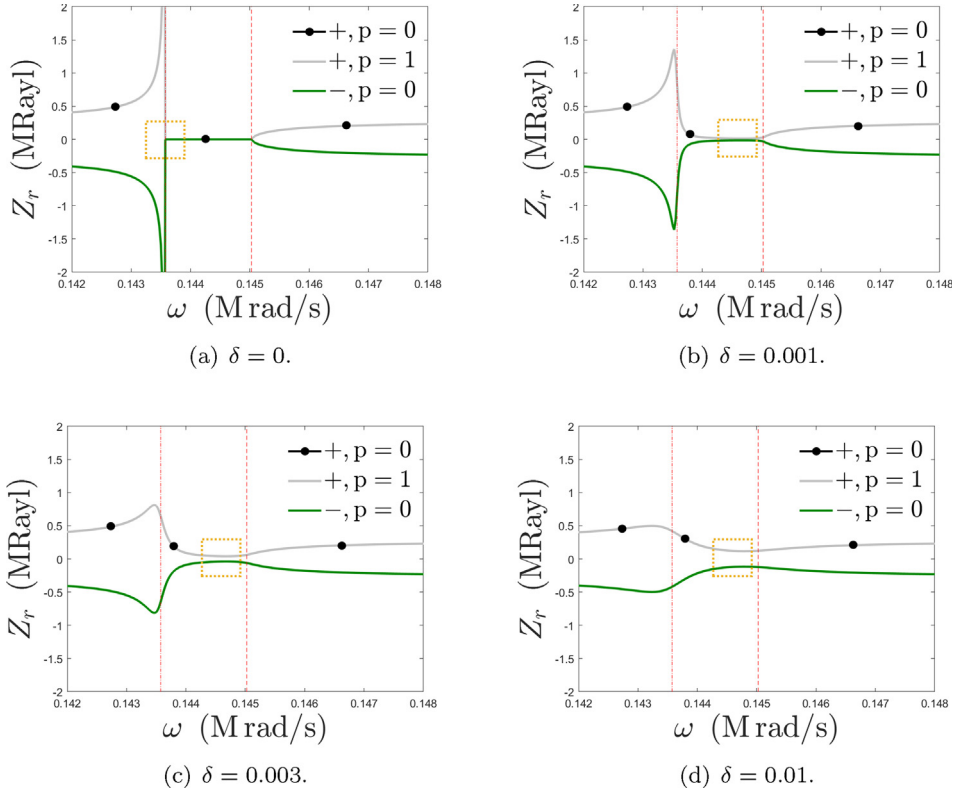

(a) $\delta = 0$. (b) $\delta = 0.001$.

(c) $\delta = 0.003$. (d) $\delta = 0.01$.

Fig. 38. Demonstration that for a 5LD unit cell with loss, Z_r cannot continuously transition from positive to negative branches in I_w.

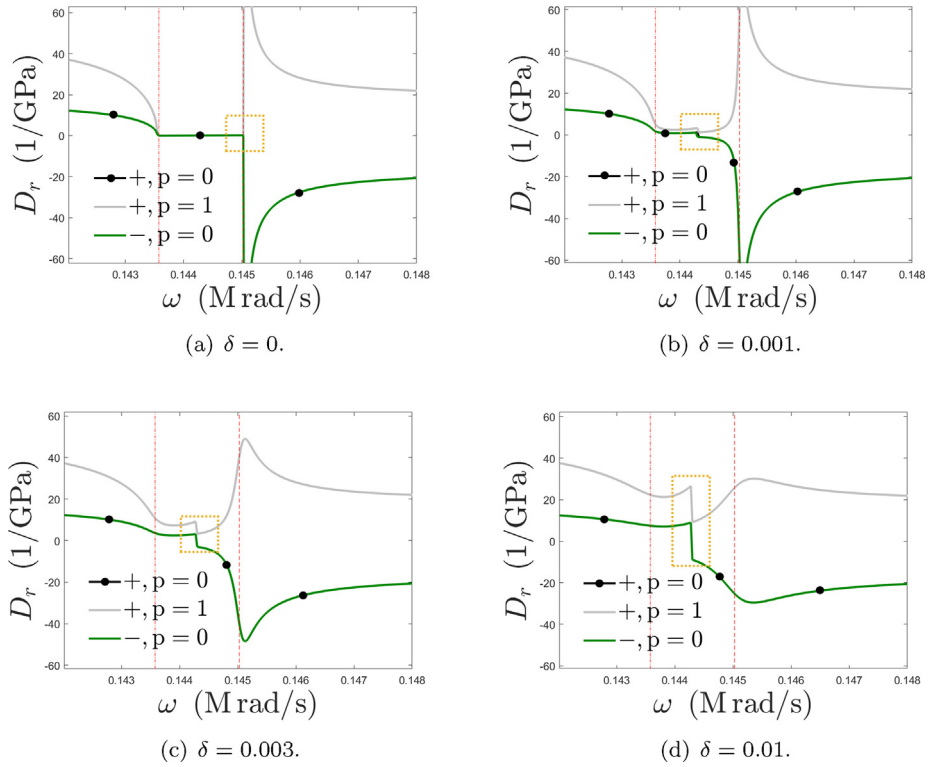

(a) $\delta = 0$. (b) $\delta = 0.001$.

(c) $\delta = 0.003$. (d) $\delta = 0.01$.

Fig. 39. Demonstration that for a 5LD unit cell with loss, D_r suffers a jump if solution transitions from 0 positive to negative branch in I_w.

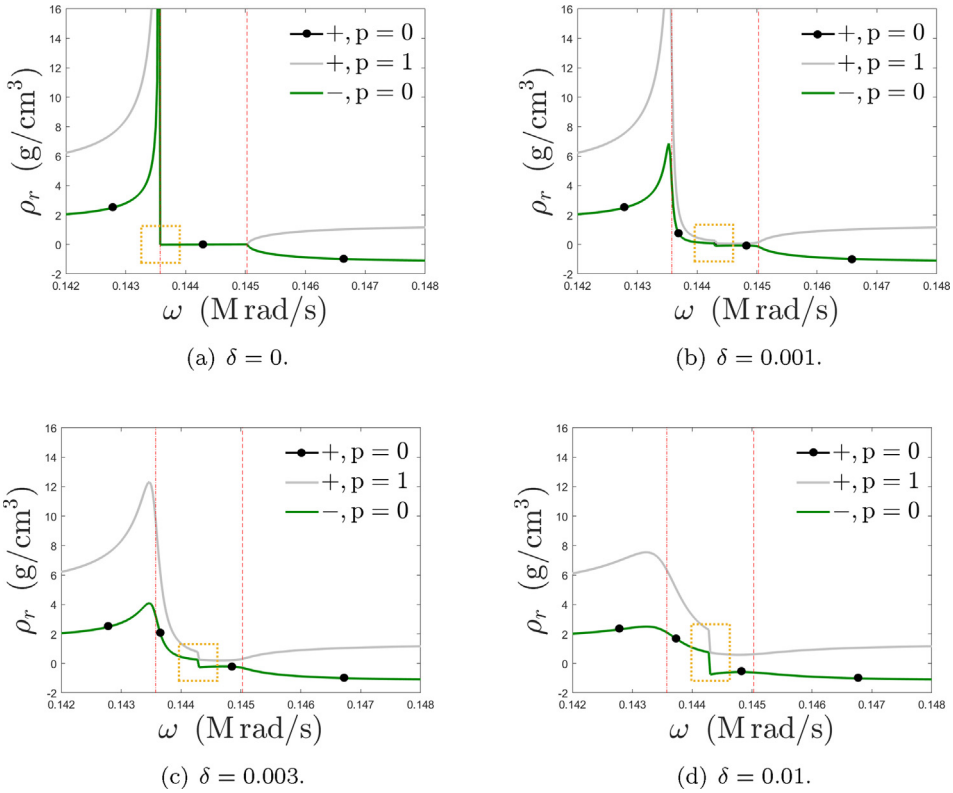

(a) $\delta = 0$. (b) $\delta = 0.001$.

(c) $\delta = 0.003$. (d) $\delta = 0.01$.

Fig. 40. Demonstration that for a 5LD unit cell with loss, ρ_r suffers a jump if solution transitions from 0 positive to negative branch in I_w.

to argue that $+, p = 1$ is the stable solution branch in I_w. Otherwise, negative k_i for $+, p = 0$ cannot undergo a jump and become positive to facilitate a switch to the $-, p = 0$ branch at any frequency.

A similar argument can be made using Z_r in Fig. 38. As shown in Fig. 38(a), for the lossless unit cell, Z_r suffers a jump at $\omega_{0.5'}$; positive and negative solution branches result in positive and negative infinite limits for Z_r in the preceding pass-band, while in the first half-cycle stop-band $Z_r = 0$ for all solution branches. This jump is shown by the dotted orange square in the figure. As discussed before, the introduction of loss, smoothen outs Z_r. As shown in Fig. 20(b), the switch from $+, p = 0$ to $+, p = 1$ occurs somewhere in the second half of the stop-band. As shown, $+, p = 0$ and $+, p = 1$ share the same solution for Z_r, thus upon the transition between the branches, Z_r remains continuous. In contrast, once loss is added, while positive and negative branch solutions for Z_r get close (shown by dotted squares), the solution cannot continuously transition from the $+, 0$ to $-, 0$ branch.

Finally, in Figs. 39 and 40 the continuity of retrieved properties for lossy unit cell is used to again argue that $+, p = 1$ is the stable solution branch. In Fig. 39(a) and 40(a), D_r and ρ_r are shown for the lossless unit cell. From (10) and that $|Z| \to \infty$ and 0 at the start and end of the stop-band, D_r and ρ_r are discontinuous at the end and start of the stop-band, respectively, as shown by dotted squares. Once loss is introduced, these retrieved parameters are smoothened out and become continuous. The retrieved parameters for $+, p = 0$ and $-, p = 0$ coincide and they suffer jumps around the center of the stop-band, shown by dotted rectangles in Fig. 39(b–d) and 40(b-d). Clearly, the retrieved parameters remain continuous by switching from $+, p = 0$ to $+, p = 1$ branches at these points, the same locations where ϕ exceeds π in Fig. 20(b).

References

Abedi, Reza, 2010. Spacetime damage-based cohesive model for elastodynamic fracture with dynamic contact (Ph.D. thesis). Department of Theoretical and Applied Mechanics, University of Illinois at Urbana–Champaign..

Abedi, R., 2017. An adaptive time domain approach to characterize dispersive elastodynamic media. In: Proceedings of ASME 2017 International Mechanical Engineering Congress & Exposition IMECE 2017, page V013T01A006 (7 pages), Tampa, Florida, USA..

Abedi, R., Mudaliar, S., 2017. A spacetime adaptive approach to characterize complex dispersive media. In Proceedings of 32nd International Union of Radio Science General Assembly & Scientific Symposium (URSI GASS), Palais des congres, Montreal, Canada, August 19–26, 2017. paper no. 2439 (4 pages)..

Abedi, R., Mudaliar, S., 2017. An asynchronous spacetime discontinuous Galerkin finite element method for time domain electromagnetics. J. Comput. Phys. 351 (Suppl. C), 121–144.

Abedi, Reza, Chung, Shuo-Heng, Erickson, Jeff, Fan, Yong, Garland, Michael, Guoy, Damrong, Haber, Robert, Sullivan, John M., Thite, Shripad, Zhou, Yuan, 2004. Spacetime meshing with adaptive refinement and coarsening. In: Proceedings of the Twentieth Annual Symposium on Computational Geometry, SCG '04. pp. 300–9, Brooklyn, New York, USA, June 9–11 2004. ACM..

Abedi, Reza, Haber, Robert B., Petracovici, Boris, 2006. A spacetime discontinuous Galerkin method for elastodynamics with element-level balance of linear momentum. Comput. Methods Appl. Mech. Eng. 195, 3247–3273.

Abedi, R., Haber, R.B., Thite, S., Erickson, J., 2006. An h–adaptive spacetime–discontinuous Galerkin method for linearized elastodynamics. Eur. J. Comput. Mech. 15 (6), 619–642.

Aghighi, Fateme, Morris, Joshua, Amirkhizi, Alireza V., 2019. Low-frequency microstructured mechanical metamaterials. Mech. Mater. 130, 65–75.

Amirkhizi, Alireza V., 2017. Homogenization of layered media based on scattering response and field integration. Mech. Mater. 114, 76–87.

Amirkhizi, Alireza V., Alizadeh, Vahidreza, 2018. Overall constitutive description of symmetric layered media based on scattering of oblique SH waves. Wave Motion 83, 214–226.

Amirkhizi, Alireza V., Nemat-Nasser, Sia, 2008. Microstructurally-based homogenization of electromagnetic properties of periodic media. Comptes Rendus Mecanique 336 (1–2), 24–33.

Andrianov, Igor V., Bolshakov, Vladimir I., Danishevs'kyy, Vladyslav V., Weichert, Dieter, 2008. Higher order asymptotic homogenization and wave propagation in periodic composite materials. Proc. R. Soc. London A 464 (2093), 1181–1201.

Arslanagić, S., Hansen, T.V., Mortensen, N.A., Gregersen, A.H., Sigmund, O., Ziolkowski, R.W., Breinbjerg, O., 2013. A review of the scattering-parameter extraction method with clarification of ambiguity issues in relation to metamaterial homogenization. IEEE Antennas Propag. Mag. 55 (2), 91–106.

Auriault, J.-L., Boutin, C., 2012. Long wavelength inner-resonance cut-off frequencies in elastic composite materials. Int. J. Solids Struct. 49 (23–24), 3269–3281.

Auriault, Jean-Louis, Boutin, Claude, Geindreau, Christian, 2010. Homogenization of Coupled Phenomena in Heterogenous Media, vol. 149. John Wiley & Sons.

Boutin, C., Auriault, J.L., 1993. Rayleigh scattering in elastic composite materials. Int. J. Eng. Sci. 31 (12), 1669–1689.

Busch, Kurt, König, Michael, Niegemann, Jens, 2011. Discontinuous Galerkin methods in nanophotonics. Laser Photon. Rev. 5 (6), 773–809.

Chan, C.T., Yu, Q.L., Ho, K.M., 1995. Order-N spectral method for electromagnetic waves. Phys. Rev. B 51 (23), 16635.

Chen, Xudong, Grzegorczyk, Tomasz M., Wu, Bae-Ian, Pacheco Jr., Joe, Kong, Jin Au, 2004. Robust method to retrieve the constitutive effective parameters of metamaterials. Phys. Rev. E 70, (1) 016608.

Chen, Xudong, Wu, Bae-Ian, Kong, Jin Au, Grzegorczyk, Tomasz M., 2005. Retrieval of the effective constitutive parameters of bianisotropic metamaterials. Phys. Rev. E 71 (4).

Craster, R.V., Kaplunov, J., Pichugin, A.V., 2010. High-frequency homogenization for periodic media. Proc. R. Soc. London A 466 (2120), 2341–2362.

Dontsov, E.V., Tokmashev, R.D., Guzina, B.B., 2013. A physical perspective of the length scales in gradient elasticity through the prism of wave dispersion. Int. J. Solids Struct. 50 (22–23), 3674–3684.

Fokin, V., Ambati, M., Sun, Cheng, Zhang, Xiang, 2007. Method for retrieving effective properties of locally resonant acoustic metamaterials. Phys. Rev. B 76, (14) 144302.

Guzina, Bojan B, Meng, Shixu, Oudghiri-Idrissi, Othman, 2019. A rational framework for dynamic homogenization at finite wavelengths and frequencies. Proc. R. Soc. A 475 (2223), 20180547.

Hasar, U.C., Barroso, J.J., Karacali, T., Ertugrul, M., 2015. Reference-plane-invariant and thickness- and branch-index-independent retrieval of effective parameters of bi-anisotropic metamaterials. AIP Adv. 5 (1).

Hui, Tong, Oskay, C., 2013. A nonlocal homogenization model for wave dispersion in dissipative composite materials. Int. J. Solids Struct. 50 (1), 38–48.

Hui, Tong, Oskay, Caglar, 2014. A high order homogenization model for transient dynamics of heterogeneous media including micro-inertia effects. Comput. Methods Appl. Mech. Eng. 273, 181–203.

Hui, Tong, Oskay, Caglar, 2015. Laplace-domain, high-order homogenization for transient dynamic response of viscoelastic composites. Int. J. Numer. Meth. Eng. 103 (13), 937–957.

Lerat, J.-M., Mallejac, N., Acher, O., 2006. Determination of the effective parameters of a metamaterial by field summation method. J. Appl. Phys. 100, (8) 84908.

Liu, Ruopeng, Cui, Tie Jun, Huang, Da, Zhao, Bo, Smith, David R., 2007. Description and explanation of electromagnetic behaviors in artificial metamaterials based on effective medium theory. Phys. Rev. E 76 (2).

Markoš, Peter, Soukoulis, C.M., 2003. Transmission properties and effective electromagnetic parameters of double negative metamaterials. Opt. Express 11 (7), 649–661.

Meng, Shixu, Guzina, Bojan B., 2018. On the dynamic homogenization of periodic media: Willis' approach versus two-scale paradigm. Proc. R. Soc. A 474 (2213). 20170638.

Merheb, B., Deymier, P.A., Jain, M., Aloshyna-Lesuffleur, M., Mohanty, S., Berker, A., Greger, R.W., 2008. Elastic and viscoelastic effects in rubber/air acoustic band gap structures: a theoretical and experimental study. J. Appl. Phys. 104 (6), 9. 064913.

Milton, Graeme W., Willis, John R., 2007. On modifications of newton's second law and linear continuum elastodynamics. In: Proceedings of the Royal Society of London A: Mathematical, Physical and Engineering Sciences, vol. 463. pp. 855–80. The Royal Society..

Mokhtari, Amir Ashkan, Lu, Yan, Srivastava, Ankit, 2019. On the emergence of negative effective density and modulus in 2-phase phononic crystals. J. Mech. Phys. Solids 126, 256–271.

Mokhtari, A.A., Lu, Y., Zhou, Q., Amirhizi, A.V., Srivastava, A., 2020. Scattering of in-plane elastic waves at metamaterial interfaces. Int. J. Eng. Sci. 150, 103278. https://doi.org/10.1016/j.ijengsci.2020.103278.

Nemat-Nasser, Sia, 2019. Inherent negative refraction on acoustic branch of two dimensional phononic crystals. Mech. Mater. 132, 1–8.

Nemat-Nasser, S., Hori, M., 2013. Micromechanics: Overall Properties of Heterogeneous Materials. Elsevier, Amsterdam, New York.

Nemat-Nasser, Sia, Srivastava, Ankit, 2011. Negative effective dynamic mass-density and stiffness: micro-architecture and phononic transport in periodic composites. AIP Adv. 1, (4) 041502.

Nemat-Nasser, Sia, Willis, John R., Srivastava, Ankit, Amirkhizi, Alireza V., 2011. Homogenization of periodic elastic composites and locally resonant sonic materials. Phys. Rev. B 83 (10), 104103.

Nemat-Nasser, Sia, Willis, John R., Srivastava, Ankit, Amirkhizi, Alireza V., 2011. Homogenization of periodic elastic composites and locally resonant sonic materials. Phys. Rev. B 83, (10) 104103.

Nicolson, A.M., Ross, G.F., 1970. Measurement of the intrinsic properties of materials by time-domain techniques. IEEE Trans. Instrum. Meas. 19 (4), 377–382.

Niegemann, J., Pernice, W., Busch, Kurt, 2009. Simulation of optical resonators using DGTD and FDTD. J. Opt. A 11 (11). 114015.

Norris, Andrew N., Shuvalov, A.L., Kutsenko, A.A., 2012. Analytical formulation of three-dimensional dynamic homogenization for periodic elastic systems. Proc. R. Soc. A 468 (2142), 1629–1651.

Orfanidis, Sophocles J., 2014. Electromagnetic waves and antennas..

Pham, K., Kouznetsova, V.G., Geers, M.G.D., 2013. Transient computational homogenization for heterogeneous materials under dynamic excitation. J. Mech. Phys. Solids 61 (11), 2125–2146.
Pors, A., Tsukerman, I., Bozhevolnyi, S.I., 2011. Effective constitutive parameters of plasmonic metamaterials: homogenization by dual field interpolation. Phys. Rev. E 84 (1), 9. 016609.
Sadeghi, H., Srivastava, A., Nemat-Nasser, S., 2013. Acoustic impedance matching using dynamic homogenization of periodic composites. Proc. SPIE 8689, Behavior and Mechanics of Multifunctional Materials and Composites 8689:86891A–86891A–8..
Santosa, Fadil, Symes, William W., 1991. A dispersive effective medium for wave propagation in periodic composites. SIAM J. Appl. Math. 51 (4), 984–1005.
Shi, Yan, Li, Zhi-Yi, Li, Long, Liang, Chang-Hong, 2016. An electromagnetic parameters extraction method for metamaterials based on phase unwrapping technique. Waves Random Complex Media 26 (4), 417–433.
Silveirinha, M.G., 2011. Time domain homogenization of metamaterials. Phys. Rev. B 83 (16), 10. 165104.
Silveirinha, Mário G., 2011. Time domain homogenization of metamaterials. Phys. Rev. B 83, (16) 165104.
Smith, David R., Pendry, John B., 2006. Homogenization of metamaterials by field averaging. JOSA B 23 (3), 391–403.
Smith, D.R., Vier, D.C., Kroll, N., Schultz, S., 2000. Direct calculation of permeability and permittivity for a left-handed metamaterial. Appl. Phys. Lett. 77 (14), 2246–2248.
Smith, D.R., Schultz, S., Markoš, P., Soukoulis, C.M., 2002. Determination of effective permittivity and permeability of metamaterials from reflection and transmission coefficients. Phys. Rev. B 65, (19) 195104.
Smith, D.R., Vier, D.C., Koschny, Th., Soukoulis, C.M., 2005. Electromagnetic parameter retrieval from inhomogeneous metamaterials. Phys. Rev. E 71, 036617.
Srivastava, Ankit, 2015. Elastic metamaterials and dynamic homogenization: a review. Int. J. Smart Nano Mater. 6 (1), 41–60.
Srivastava, Ankit, Nemat-Nasser, Sia, 2011. Overall dynamic properties of three-dimensional periodic elastic composites. Proc. R. Soc. A 468 (2137), 269–287.
Wang, Ze-Ping, Sun, C.T., 2002. Modeling micro-inertia in heterogeneous materials under dynamic loading. Wave Motion 36 (4), 473–485.
Wang, Zhi Guo, Lee, Sam Hyeon, Kim, Chul Koo, Park, Choon Malm, Nahm, Kyun, Nikitov, S.A., 2008. Effective medium theory of the one-dimensional resonance phononic crystal. J. Phys.: Condens. Matter 20, (5) 055209.
Wautier, Antoine, Guzina, Bojan B., 2015. On the second-order homogenization of wave motion in periodic media and the sound of a chessboard. J. Mech. Phys. Solids 78, 382–414.
Weir, William B, 1974. Automatic measurement of complex dielectric constant and permeability at microwave frequencies. Proc. IEEE 62 (1), 33–36.
Willis, J.R., 2009. Exact effective relations for dynamics of a laminated body. Mech. Mater. 41 (4), 385–393.
Willis, J.R., 2011. Effective constitutive relations for waves in composites and metamaterials. Proc. R. Soc. A 467 (2131), 1865–1879.
Willis, J.R., 2012. The construction of effective relations for waves in a composite. C. R. Mec. 340 (4–5), 181–192.
Willis, John R., 2016. Negative refraction in a laminate. J. Mech. Phys. Solids 97, 10–18.
Zhu, R., Huang, G.L., Hu, G.K., 2012. Effective dynamic properties and multi-resonant design of acoustic metamaterials. J. Vib. Acoust. Trans. ASME 134 (3).